frontiers | Frontiers in Photonics

TYPE Review
PUBLISHED 27 February 2024
DOI 10.3389/fphot.2024.1359784

Check for updates

OPEN ACCESS

EDITED BY
Wenfeng Xia,
King's College London, United Kingdom

REVIEWED BY
Mengjie Shi,
King's College London, United Kingdom
Yayao Ma,
University of California, Los Angeles, United States

*CORRESPONDENCE
Marvin Doyley,
mdoyley@ur.rochester.edu
Jun Xia,
junxia@buffalo.edu

†These authors have contributed equally to this work

RECEIVED 22 December 2023
ACCEPTED 12 February 2024
PUBLISHED 27 February 2024

CITATION
Nyayapathi N, Zheng E, Zhou Q, Doyley M and Xia J (2024), Dual-modal photoacoustic and ultrasound imaging: from preclinical to clinical applications.
Front. Photonics 5:1359784.
doi: 10.3389/fphot.2024.1359784

COPYRIGHT
© 2024 Nyayapathi, Zheng, Zhou, Doyley and Xia. This is an open-access article distributed under the terms of the Creative Commons Attribution License (CC BY). The use, distribution or reproduction in other forums is permitted, provided the original author(s) and the copyright owner(s) are credited and that the original publication in this journal is cited, in accordance with accepted academic practice. No use, distribution or reproduction is permitted which does not comply with these terms.

Dual-modal photoacoustic and ultrasound imaging: from preclinical to clinical applications

Nikhila Nyayapathi[1†], Emily Zheng[2†], Qifa Zhou[3], Marvin Doyley[1*] and Jun Xia[2*]

[1]Electrical and Computer Engineering, University of Rochester, Rochester, NY, United States, [2]Department of Biomedical Engineering, University at Buffalo, Buffalo, NY, United States, [3]Department of Biomedical Engineering, University of Southern California, Los Angeles, CA, United States

Photoacoustic imaging is a novel biomedical imaging modality that has emerged over the recent decades. Due to the conversion of optical energy into the acoustic wave, photoacoustic imaging offers high-resolution imaging in depth beyond the optical diffusion limit. Photoacoustic imaging is frequently used in conjunction with ultrasound as a hybrid modality. The combination enables the acquisition of both optical and acoustic contrasts of tissue, providing functional, structural, molecular, and vascular information within the same field of view. In this review, we first described the principles of various photoacoustic and ultrasound imaging techniques and then classified the dual-modal imaging systems based on their preclinical and clinical imaging applications. The advantages of dual-modal imaging were thoroughly analyzed. Finally, the review ends with a critical discussion of existing developments and a look toward the future.

KEYWORDS

photoacousitc imaging, ultrasound imaging, clinical applicability, preclinical studies, dual modal imaging

1 Introduction

Medical imaging plays a critical role in various aspects of patient care. Whether it is diagnostic, interventional, or surgical, medical providers rely heavily on imaging technologies to make important decisions at every stage of disease diagnosis and treatment planning. Subsequently, there has been immense innovation to make medical imaging more efficient, effective, and error-free. Imaging technologies are based on exploiting different properties of biological tissue upon its interaction with electromagnetic or acoustic waves. Each imaging modality provides unique and relevant information necessary to understand and interpret different biological contrasts. Researchers in dual-modal imaging systems aim to integrate the contrasts from different modalities for improved disease diagnosis and decision-making. In this article, we focus on one such integration—dual-modal imaging with photoacoustic (PA) and ultrasound (US) technologies. Ultrasound (US) imaging is a popular clinical tool that is portable, cost-effective, and provides real-time imaging capabilities. Photoacoustic (PA) imaging is a relatively new method that combines optical absorption and acoustic detection. Different wavelengths can be used to differentiate various tissue chromophores. The main advantage of the PA/US dual-modal imaging is the shared hardware. Both PA and US use ultrasonic transducers for acoustic detection. Thus, existing ultrasound systems can

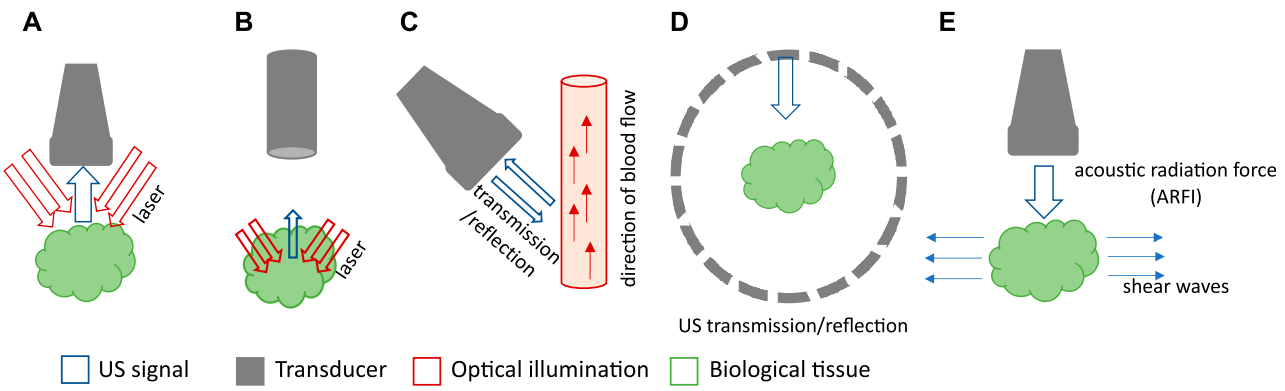

FIGURE 1
Schematic drawings of various PA and US imaging modalities. **(A)** Schematic of PACT with a linear array. **(B)** Schematic of PAM with single-element transducer and confocal light illumination. **(C)** Schematic of Doppler US. **(D)** Schematic of USCT with ring array. **(E)** Schematic of US elastography.

potentially be upgraded to PA/US systems by adding an optical source (laser, LED, etc.), thereby leading to faster clinical translation as opposed to a completely new system.

In the past few years, there are already a few reviews in the field of dual-modal photoacoustic and ultrasound imaging (Wang et al., 2020; Wen et al., 2022; Lee et al., 2023). However, they typically focused on a very specific area, such as ultrasound guided photoacoustic imaging or clinical translational imaging. In this review, we aim to provide a comprehensive overview of dual-modal PA/US systems for both preclinical and clinical applications. Section 2 provides a brief overview of the fundamental principles of photoacoustic and ultrasound imaging. In Section 3, we review various PA/US systems based on their preclinical and clinical applications. We will explain the current research progress and highlight the crucial methodologies for each research field. Section 4 briefly touches upon various advancements in PA and US. The final section also summarizes the benefits of dual-modal configurations and states existing challenges in the area.

2 Principles

Photoacoustic (PA) imaging is a hybrid imaging modality that integrates optical illumination and acoustic detection (Beard, 2011a). In PA imaging, a pulsed laser is used to induce thermal expansion in the tissue, which generates acoustic waves. This acoustic signal is measured with an ultrasound transducer and the initial distribution of light absorption is reconstructed to form an image (Attia et al., 2019). As acoustic waves scatter much less than light in tissue (Lengenfelder et al., 2019), PA imaging allows high-resolution imaging in depth beyond the optical scattering limit. When different wavelengths are used, PA can spectrally quantify a wide range of endogenous and exogenous chromophores via their spectral absorption signatures (Jacques, 2013; Wu et al., 2014). Common intrinsic chromophores include hemoglobin, melanin, lipids, and water. Since hemoglobin is one of the major components of blood, PA modality can quantify functional features of vessels such as oxygen saturation (Xia et al., 2013a) and blood flow (Wang et al., 2013). Moreover, vascular abnormalities are an early indicator of various diseases. Therefore, PA's ability to provide functional information about blood vessels through monitoring hemoglobin makes it a promising technique for a wide range of clinical applications (Hu and Wang, 2010). Exogenous chromophores refer to chemical dyes or nanoparticles that can be introduced into the body. They improve PA imaging contrast and/or serve as targeting agents for molecular imaging (Luke et al., 2012a; Luke et al., 2012b).

Photoacoustic tomography (PAT) can be majorly classified into three categories based on its applications: photoacoustic computed tomography (PACT), photoacoustic microscopy (PAM) and photoacoustic endoscopy (PAE) (Wang, 2008a; Beard, 2011a; Wang, 2017). PA computed tomography (PACT), is based on the reconstruction of acoustic waves generated from the photoacoustic source (Figure 1A). In general, an unfocused ultrasonic transducer array is scanned over the source to generate an image (Wang, 2008b). PA microscopy (PAM), on the other hand, employs raster-scanning of optical and acoustic foci (focused single-element transducer) and forms images directly from acquired depth-resolved signals (Yao and Wang, 2013). PAM maximizes its detection sensitivity by confocally aligning its optical illumination and acoustic detection (Figure 1B). While the axial resolution of PAM is primarily determined by the imaging depth and the frequency response of the ultrasonic transducer, its lateral resolution is determined by the combined point spread function of the dual foci (Yao and Wang, 2013). Photoacoustic endoscopy (PAE) is a variation of PAM for internal organ imaging, which uses rotational scanning (Wang and Hu, 2012). Detailed reviews of different PA implementations can be found in (Xia et al., 2014; Zhou et al., 2016; Wang, 2017).

Conventional ultrasound (US) imaging typically operates in reflection or pulse-echo mode. A US image is obtained by transmitting acoustic waves in tissue and detecting reflected echoes to locate the target. As acoustic reflection is induced by impedance mismatch among tissue structures, ultrasound imaging provides insight into tissue morphology and properties. Depending on the application, researchers have combined photoacoustic imaging with various ultrasound-based techniques such as reflection-mode ultrasound, ultrasound computed tomography (USCT), ultrasound elastography, and Doppler ultrasound. Doppler ultrasound utilizes shifts in ultrasound frequencies,

TABLE 1 PA and US imaging characteristics.

	Resolution	Depth	Contrast
PACT (Wang, (2009))	~50 μm ~1 mm	~1–10 cm	Tissue optical absorption
PAM (Wang, (2009))	~0.5–50 μm	~1–10 mm	Tissue optical absorption
Ultrasound (Szabo, (2004))	~50 μm ~1 mm	~1–10 cm	Difference in acoustic impedance among tissues
US Doppler (Poelma, (2017))	~0.5–2 mm	~1mm - 10 cm	US frequency shift (blood flow)
US microDoppler (Christensen-Jeffries et al., 2020)	~10–200 μm	~1mm - 2 cm	Blood flow in microvasculature
USCT (Duric et al., 2005)	~50 μm - 1 mm	~1cm - 10 cm	Acoustic attenuation and speed of sound
US elastography (Ormachea and Parker, (2020))	~50 μm - 2 mm	~1–10 cm	Tissue stiffness

TABLE 2 Oncology.

Application	PA characteristics	US characteristics
Oncology	Total concentration of hemoglobin (CHb) of tumor Oxygen saturation of hemoglobin (sO_2) of tumor Peripheral vasculature	Tumor boundary
		Shape
		Echogenicity
		Acoustic enhancement/shadowing

caused by the movement of hemoglobin molecules, to quantify the speed and direction of blood flow (Figure 1C) (Szabo, 2004). USCT is a transmission-mode approach that can reveal distributions of the speed of sound (SOS) and acoustic attenuation of tissue, leading to more comprehensive tissue characterization (Figure 1D) (Li et al., 2009). Ultrasound elastography involves perturbing the tissue using a quasi-static, harmonic, or transient mechanical source and then tracking the internal tissue displacements to deduce the stiffness information (Figure 1E) (Gennisson et al., 2013). Similar to PA, ultrasound can also be implemented as ultrasound tomography (Watson, 2022), ultrasound microscopy (Couture et al., 2018), or ultrasound endoscopy systems (Ang et al., 2018). Table 1 highlights the key features, imaging depth, and spatial resolution of each modality.

Combining PA and ultrasound imaging is an obvious choice, as most of the equipment remains the same. PA/US dual-modal configurations can provide a more comprehensive evaluation of the target tissue than stand-alone PA or US modality. In the following section, we will review the various PA/US techniques and highlight their applications in the preclinical and clinical space.

3 Applications

3.1 Oncology

Cancer is a substantial public health problem worldwide (Siegel et al., 2019). Early detection of cancer would significantly increase the success rate of the treatment and patient survival. The analysis of tumor microenvironment can reveal its behavior and growth pattern. One such key feature is tumor angiogenesis, which is the formation of new blood vessels around the tumor region (Kerbel, 2008). In addition, most tumors are prone to hypoxia during their growth. It is caused by insufficient blood supply to the tumor region (Hockel and Vaupel, 2001). Hypoxia can be: 1) diffusion-limited (permanent hypoxia) in areas far away from blood vessels; or 2) perfusion-limited which is caused by leaky and irregular capillary growth in tumors (Rofstad et al., 2007). Morphological features of tumors include stiffness, heterogeneity, anisotropy, etc. (Masuzaki et al., 2007; Partridge et al., 2010; Seewaldt, 2014). While MRI and CT have been widely used in the clinic for cancer imaging, PA/US dual-modal systems have unique advantages due to their non-invasiveness, low cost, and radiation-free nature. Therefore, several groups have used PA/US imaging for different types of cancer applications. Table 2 summarizes the PA and US characteristics for oncological applications.

3.1.1 Preclinical imaging

Various dual-modal small animal imaging systems have been proposed for pre-clinical cancer imaging and research. Merčep et al., 2019 designed a hybrid transmission-reflection optoacoustic ultrasound (TROPUS) system shown in Figure 2A. Transmission USCT provided speed of sound and acoustic attenuation maps, while reflection USCT and PA provided optical absorption and acoustic reflectivity. Overall, this technique revealed vascularization, organ parenchyma, tissue reflectivity, density, and stiffness in live mice (Figures 2B–E). With this dual-modal approach, results from one modality could be used as an *a priori* knowledge to enhance the reconstruction of another. For instance, the speed of sound maps can be used to enhance PA image reconstruction to render sharper PA features.

To understand the vascular morphology and functionality in the tumor microenvironment, Bar-Zion et al., 2016 used dynamic contrast-enhanced ultrasound (DCEUS) and dual-wavelength photoacoustic imaging as a tool to monitor anti-vascular treatment. In different murine tumor models, the DCEUS system

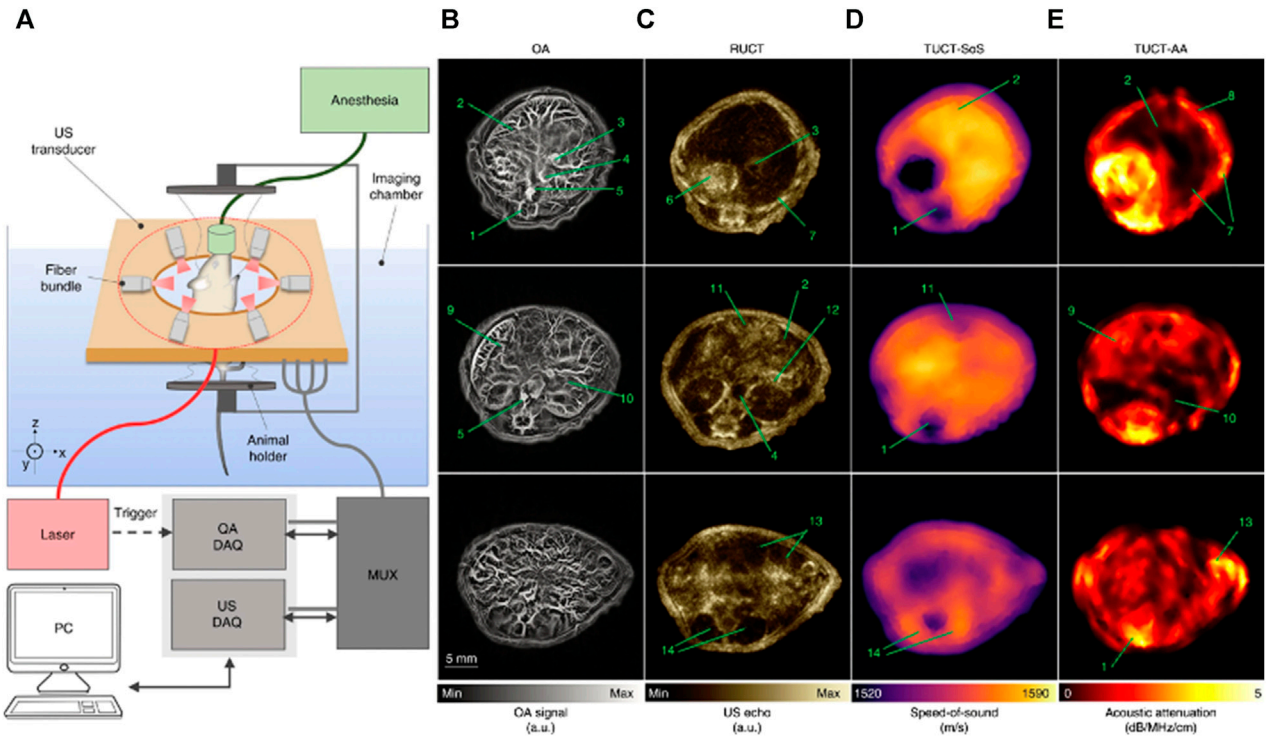

FIGURE 2
(A) A schematic of transmission-reflection ultrasound optoacoustic system (TROPUS) **(B)** Representative cross-sections acquired in the optoacoustic mode. **(C)** The corresponding reflection-mode ultrasound images. **(D and E)** The corresponding transmission-mode ultrasound images show the distribution of the speed of sound and acoustic attenuation, respectively. Annotations: 1: spinal cord; 2: liver; 3: vena porta; 4: vena cava; 5: aorta; 6: stomach; 7: ribs; 8: skin/fat layer; 9: spleen; 10: right kidney; 11: cecum; 12: pancreas; 13: intestines; 14: muscle. Reproduced with permission from (Merčep et al., 2019).

detected changes in perfusion using gas-filled microbubbles as acoustic contrast, whereas PA imaging measured oxygenation and hemoglobin levels. Combining the two modalities, viable and necrotic tissue could be distinguished from hemorrhagic regions, resulting from leaky capillaries. However, the system is only capable of 2D imaging with low resolution and poor sO_2 separation for low values.

Besides cancer screening and diagnosis, PA/US can also be used to monitor the response to treatment. Radiation therapy is widely used in cancer treatment which involves inducing cancer cell death by disrupting the DNA via ionizing radiation. Endothelial cell damage within the tumor microvasculature is another effect of radiation (Garcia-Barros et al., 2003). Ultrasound-stimulated microbubbles have been demonstrated as radiation enhancers. To investigate the extent of microvascular disruption caused by radiation therapy using US-stimulated microbubbles, Briggs et al., 2014 used PA imaging and US power Doppler to study the oxygen saturation and therapy response. PA was used to detect oxygen saturation and power Doppler imaging was used to assess blood flow. In a murine pancreatic model designed to distinguish responders from non-responders to photodynamic therapy, Mallidi et al., 2015 used US to identify the tumor region and obtain B-scans while multi-wavelength PA to obtain sO_2 images of the tumor in a murine model with glioblastoma. The average oxygen saturation (sO_2) was calculated before and after therapy to predict tumor reoccurrence.

3.1.2 Clinical imaging

3.1.2.1 Breast cancer

Breast cancer has the highest mortality rate in cancer-related deaths in women (Jemal et al., 2011). To achieve good resolution, deep penetration and large field of view, different groups used different detection geometries, as discussed by Nyayapathi and Xia, 2019; Manohar and Dantuma, 2019; Das et al., 2021; Kratkiewicz et al., 2022 have also provided comprehensive reviews on this topic. In most of these systems, PA is used to obtain breast vasculature and oxygen saturation, while US provides tissue morphology. The additional functional information obtained by PA would be useful to assess tumor microenvironment and growth rate, thus reducing unnecessary biopsies. Furthermore, monitoring changes in tumor vasculature can also be a useful tool in monitoring therapy response and provide tailor made treatment plans.

Recently, Seno Medicals received FDA approval for Imagio®, their handheld PA/US imaging system (Stephens, 2021). This system provides two modes: 1) US mode for real-time grayscale images, and 2) PA/US mode for functional information overlaid on grayscale US. PA/US mode, which uses dual lasers (755 nm and 1,064 nm), generates oxy- and deoxy-hemoglobin maps as shown in Figures 3A–C (Oraevsky et al., 2018a). Multicenter clinical trials were conducted in the United States (Neuschler et al., 2018) and Netherlands (Maestro) (Menezes et al., 2018). Results from the trials indicate that the specificity of PA/US was 14.9% higher than US

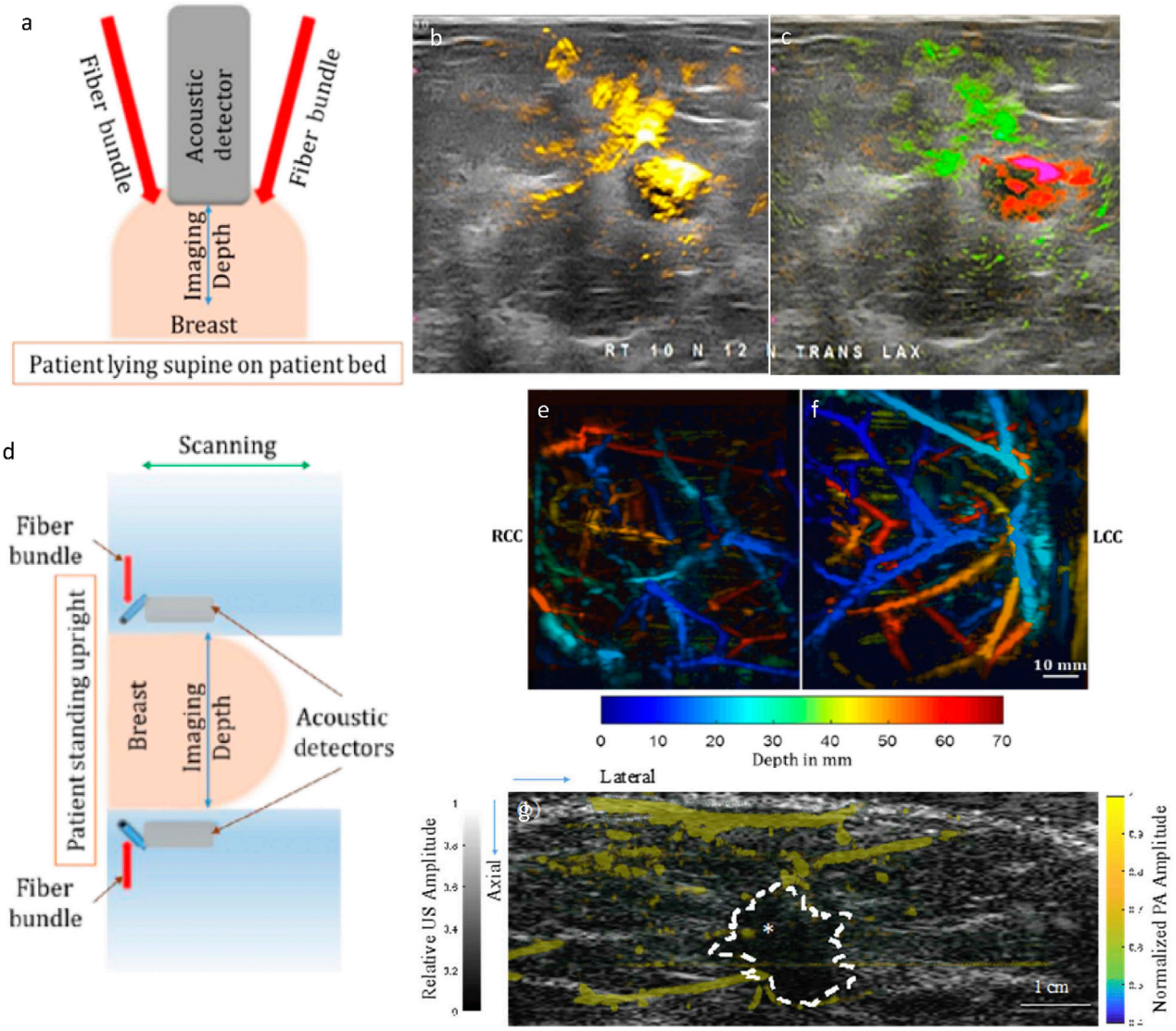

FIGURE 3
(A) A schematic of the handheld imaging system. **(B)** and **(C)** Optoacoustic functional images upgraded radiologist interpretation to BI-RADS 5 (highly suspicious for malignancy) from BI-RADS 3 (probably benign) based on conventional ultrasonic morphological images. **(B)** The PA total hemoglobin map is shown in yellow and subjected to a threshold. **(C)** The PA relative map shows oxygenated blood in green and relatively deoxygenated blood in red and is not subjected to a threshold. **(D)** A schematic of Dual Scan Mammoscope (DSM). PA depth-encoded MIP image of a volunteer with scattered fibroglandular breast density and thickness after compression of 7 cm (craniocaudal view): **(E)** right breast, **(F)** left breast. **(G)** PA and US images from a 50-year-old patient with invasive ductal carcinoma, SBR grade II with scattered fibroglandular breast density. The tumor mass is marked with an asterisk. Grayscale US was acquired from DSM. PA features are shown in color scale as they represent the hemoglobin map in the breast: stronger PA amplitudes indicate a higher concentration of hemoglobin. Most PA features are concentrated at the periphery of the tumor. Reproduced with permission from (Oraevsky et al., 2018a; Nyayapathi and Xia, 2019; Nyayapathi et al., 2021). © 2021 Optica Publishing Group © 2020 IEEE.

alone, and sensitivity was comparable (PA/US = 96%; US = 98.6%). Moreover, this PA/US system was able to downgrade (from BI-RADS 4A to 3 or lower; BI-RADS 3 to 2) 34.5% of benign masses and upgrade (from BI-RADS 3–4A or higher)) 47% of malignant masses in comparison to US (Neuschler et al., 2018). Here, Breast imaging and reporting data system, or BI-RADS is a standard diagnostic tool used to standardize terminology and report tumor grade classification across various imaging platforms (Pesce et al., 2019).

PA/US tomography systems, when compared to their handheld counterparts, have the advantage of being operator independent. To this date, three dual-modal PA/US breast tomography systems have been developed. First, the Kyoto-Canon PAM-02 system used a 600-element rectangular grid CMUT array for PA acquisition with 2 MHz central frequency (Asao et al., 2016). A separate linear array transducer (central frequency: 6 MHz) was used to obtain pulse-echo US data. PA was used to generate hemoglobin saturation maps from 756 nm to 797 nm (Figure 3B). Craniocaudal and mediolateral oblique imaging views were obtained. Second, Oraevsky et al., 2018b developed and arc-shaped array-based system called LOUISA-3D (laser optoacoustic imaging system assembly) to rotationally scan the breast. The pendant breast is imaged using two wavelengths (757 nm and 797 nm) to obtain

oxygen saturation as well as the hemoglobin map. However, this system used two different transducers for US and PA acquisition, thus the imaging speed is relatively slow. Third, Nyayapathi et al., 2019 developed a system with two linear arrays to scan the breast in the craniocaudal plane, called the dual-scan mammoscope or DSM (shown in Figures 3D–F). The DSM is a dual transducer imaging system that simultaneously acquired PA and US images and therefore obtained naturally co-registered images. The DSM was able to acquire PA features of the tumor region based on the tumor subtype (Nyayapathi et al., 2021) (see Figure 3G). In the next iteration (DSM-2), Zheng et al., 2021 improved resolution and incorporated quasi-static ultrasound elastography for better tissue characterization. However, with single wavelength illumination, this system is only able to obtain the total hemoglobin map.

3.1.2.2 Thyroid cancer

As thyroid nodules are detected in about 60% of healthy subjects, the primary goal in screening for thyroid cancer is to detect thyroid cancer accurately and avoid unnecessary biopsies (Gharib et al., 2016). Yang et al., 2017 compared PA/US imaging of thyroid nodules to color Doppler ultrasound. In comparison to color Doppler, PA could image blood vessels with slow blood flow speed and provide functional information. However, along with penetration depth, another limitation for this study was acoustic reflection artifacts due to impedance mismatch in the trachea region. Another PA/US system was developed by Kim et al., 2021 to image human thyroid nodules in real-time with the goal of reducing unnecessary biopsies. Multispectral PA imaging (690–930 nm) was performed to assess oxygen saturation along with B-mode US imaging. Also, based on the American Thyroid Association (ATA) guidelines and this multiparametric PA/US analysis, a new classification method was developed with about 40% greater specificity. However, due to carotid pulsation, breathing and other movements, motion artifacts were unavoidable.

3.1.2.3 Ovarian cancer

Another area of clinical interest is ovarian cancer, as it is the most lethal gynecological cancer [ref]. Most diagnosed women are already at the late stages of cancer due to a lack of proper early screening procedures (Clarke-Pearson, 2009; Torre et al., 2018). Various groups have made significant contributions to this field (Zhu, 2022). Amidi et al., 2019 developed a PA/US imaging system for ovarian lesions in humans. Using a transvaginal probe, pulse-echo US provided the morphological information, while PA provided functional information of the ovarian lesions. PA/US images were co-registered and benign ovaries were differentiated from patients with ovarian cancer using a generalized linear model and SVM (support vector machine). PA features (total hemoglobin, etc.) were added to improve classification results. However, a larger sample size is needed to strengthen the analysis.

Several groups are developing PA/US imaging systems to address other types of cancer as well. Kothapalli et al., 2019 developed a transrectal US and PA imaging system (TRUSPA) for prostate cancer imaging (Schröder et al., 2009; Ferlay et al., 2015; Agrawal et al., 2020). Colorectal cancer is one of the most common cancers in the United States (Siegel et al., 2017). Leng et al., 2018 combined US with acoustic resolution PAM (AR-PAM) on *ex vivo* colorectal tissue. AR-PAM relies on acoustic focusing instead of optical focusing and thus penetrates deeper than optical resolution PAM. This system was able to differentiate benign from malignant tissues. However, these systems are yet to be tested *in vivo*.

3.2 Brain imaging

The brain has various functions, such as maintaining autonomic functions, delivering sensory information, and conducting motor control, so brain-related diseases can severely affect essential body functions. Various imaging techniques have been proposed to reveal the disease-induced pathological changes of the cerebral vasculature. However, existing imaging approaches have their limitations, such as small FOV (microscopic system), poor spatial resolution (non-invasive optical modalities), low sensitivity to cellular events (MRI and CT), and low spatial resolution [positron emission tomography (PET) and single-photon emission computed tomography (SPECT)] (Razansky et al., 2021). Thus, photoacoustic has attracted increased attention because of its ability to conduct non-invasive functional imaging with high resolution and deep penetration. Applications of PA/US brain imaging include functional and molecular imaging, which allows a better understanding of brain functions and monitoring of drug delivery procedures. Furthermore, the anatomic information obtained through the US can improve the performance of PA in different aspects, including signal segmentation, focus adjustment, and the application of contrast agents for longitudinal imaging. All those applications will be covered in this section. Table 3 summarizes the PA and US characteristics for brain imaging applications.

3.2.1 Preclinical imaging

Several research groups have made significant advancements in functional brain imaging with PA/US microscopy (Ning et al., 2015a; Rebling et al., 2018a; Estrada et al., 2020a; Li et al., 2022). As shown in Figure 4A, PA/US microscopy involves a confocally aligned focused laser beam and ultrasonic transducer for co-registered high-frequency (30–35 MHz) imaging. This modality

TABLE 3 Brain imaging.

Application	PA characteristics	US characteristics
Brain imaging	Total concentration of hemoglobin (CHb)	Skull-cortex interface
	The oxygen saturation of hemoglobin (sO_2)	Skull contour
	Cerebral blood flow (CBF)	Tumor boundaries
	Accumulated contrast agent	TUS-based BBB-open procedure

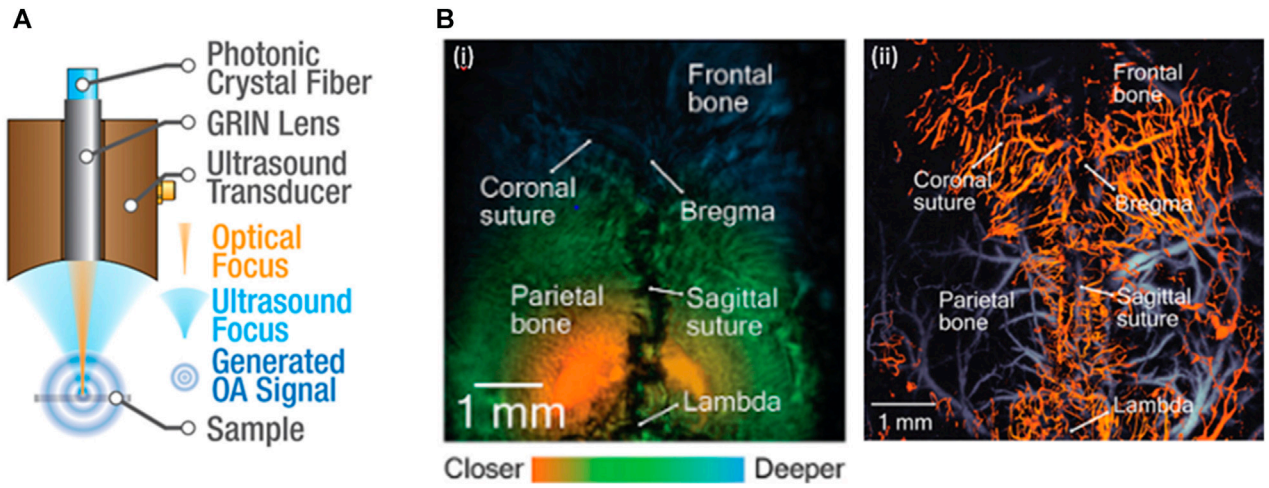

FIGURE 4
(A) A sketch of the PA/US dual modal microscopy. The PA/US microscopy can conduct co-registered PA and US imaging of the brain. **(B)** Co-registered (i) US and (ii) PA images. Based on the estimated skull thickness, the segmented vascular structure can be divided into calvarial (hot) and cerebral (cold) vascular networks. Reproduced with permission from (Ning et al., 2015b; Rebling et al., 2018b).

utilizes a laser wavelength of 532 nm for vessel mapping (Li et al., 2022). To provide additional functional information, many research groups have incorporated another wavelength in the range of 565–595 nm for spectral unmixing (Ning et al., 2015a; Rebling et al., 2018a; Estrada et al., 2020a).

One of the biggest challenges faced by stand-alone PA modality for brain imaging is the inability to differentiate signals generated by the brain from those originating from the skull (Nie et al., 2012). PA/US modality overcomes this limitation by utilizing the US-provided anatomical information for vascular segmentation, which can be accomplished by extracting the maximum signal in each A-line to map the surface contour of the skull (Ning et al., 2015a) or by combining complementary information from dual-modal imaging to estimate skull thickness and separate calvaria and cerebral vasculature networks (Rebling et al., 2018a). Furthermore, the US-provided anatomical information enables dynamic adjustment of the PAM focus. By focusing the PAM on the target cortical vasculature, the team reached a remarkable 2 μm lateral resolution on the uneven brain surface, allowing for the distinction of single capillaries (Ning et al., 2015a).

The PA/US modality integrates multispectral imaging, vessel segmentation, and dynamic focus adjustment techniques to access functional parameters of the mouse brain at the microvascular level. Experimental studies on mice have confirmed the efficacy of PA/US microscopy in multi-parametric transcranial imaging, including measurements of total hemoglobin concentration (CHb), oxygen saturation of hemoglobin (sO_2), cerebral blood flow (CBF), and cerebral metabolic rate of oxygen (CMRO2) (Ning et al., 2015a; Rebling et al., 2018a; Estrada et al., 2020a; Li et al., 2022). Figure 4B illustrates an overlaid PA/US image with US-obtained anatomical information and the corresponding vasculature obtained through PA. Subsequent studies have employed the PA/US modality with various algorithms to track changes in the morphology of vascular structures for longitudinal imaging. Potential applications of this system include monitoring the recovery of supplemental vessels in calvarial bone marrow following radiation exposure (Estrada et al., 2020a), as well as tracking abnormalities in bone vascular structures during skull bone growth in mice, which is an indicator of diseases like osteoarthritis and osteoporosis (Li et al., 2022).

Another application to aid in PA modality is drug delivery and pharmacokinetic monitoring. The blood-brain barrier (BBB) is formed by the tight junctions of endothelial cells that separate the central nervous from the brain. The BBB shields the body from pathogens and other harmful substances but also makes pharmaceutical treatment and contrast-agent-added brain imaging challenging (Zloković et al., 1985). An earlier study demonstrated that the BBB influenced the performance of PA in longitudinal imaging by clearing the injected contrast agent in a short period (Figure 5A) (Leng et al., 2019). Incorporating the acoustic technique can overcome this limit through the transcranial-focused ultrasound (TUS) BBB-open procedure. This procedure utilizes a low-frequency (<1 MHz) focused transducer with a low f-number setting, such as 1, to traverse the skull and create localized disruption, thereby opening the BBB barrier (Hartman et al., 2019). As shown in Figure 5B, combining the TUS opening procedure and contrast agents enables PAM to visualize brain tumors at late/early stages with a superior signal-to-background ratio (15.4 and 7.2, respectively) compared to MRI (Guo et al., 2017). This approach also allows for real-time imaging of individual plaques and proteins (Hartman et al., 2019). While low frequency allows TUS to transfer through the skull, it affects the system's capability to perform targeting imaging (Constans et al., 2017). A more advanced mechanical setup (Figure 5C) was proposed to address this issue (Estrada et al., 2020b). The system contains a 512-element spherical transducer with a radius curvature of 4 cm, a covering angle of 140°, and an adjustable transmission delay that allows for a 5.5 ns time resolution. Together, these features optimize the focusing capacity of the system close to the diffraction limit for highly selective imaging, and the large covering angle also makes real-time volumetric PA images across the entire murine brain possible.

Microscopic modalities in brain imaging face significant limitations in penetration depth and acquisition time. Current

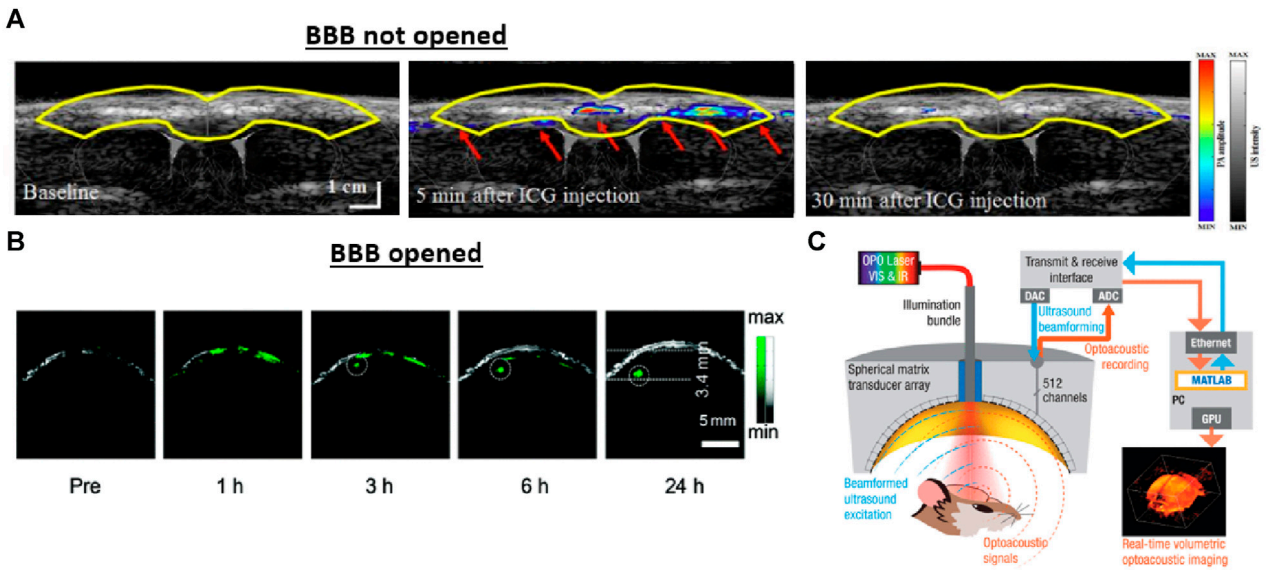

FIGURE 5
The effect of the blood-brain barrier (BBB) on longitudinal imaging and approaches for opening the BBB barrier through acoustic techniques. **(A)** An example of imaging without opening the BBB barrier. Real-time PA/US visualization results after the injection of indocyanine green (ICG) contrast agent in a coronal view. Due to the intact blood-brain barrier, the contrast through the cortical surface of the rat declined within 30 min after injection. **(B)** An imaging example with the BBB barrier opened for comparison. The overlapped PA/US images of the brain tumor were obtained at different time points following the TUS-BBB-opening procedure. The BBB opening procedure allows the applied nanoparticle to pass through the barrier and accumulate inside the tumor location for longitudinal imaging. The US modality provides structural information, such as the skin and skull margin, and the PA reveals the tumor entity marked by the applied nanoparticle. **(C)** A schematic drawing of the PA/US system for BBB opening and PA/US imaging. Transcranial-focused ultrasound was used to open the BBB, while PA/US dual-modal imaging could be performed with the same spherical array. Reproduced with permission from (Guo et al., 2017; Na et al., 2022a).

TABLE 4 Cardiology and endovascular applications.

Application	PA characteristics	US characteristics
Cardiology and Endovascular Applications	Lipid concentration in plaque	Lesion localization
	Lipid deposition and quantification	Arterial wall thickness

literature indicates a maximum penetration depth of approximately 6 mm, while the largest field of view (FoV) of 7 × 7 mm^2 requires several minutes to cover with a micro-meter level step size. These constraints pose challenges in capturing quick functional signals and reducing motion artifacts during clinical trials. Although tomographic configurations have addressed the FoV challenge to some extent (Estrada et al., 2020b), the acoustic attenuation and aberration caused by the human skull remain unresolved. However, a recent study proposed by Na et al. suggested a potential solution to this issue by utilizing numerical skull models to correct skull-induced acoustic aberration (Na et al., 2022a). The team stated that a signal-to-noise ratio of 77 at a depth of around 10 mm below the cortical surface is theoretically achievable. Recently, Tang et al., 2023 used a spherically focused 2D array for combined PA and ULM imaging of the brain. The deep vascular structures obtained from ULM can be overlaid on top of the functional PA image for comprehensive study of the brain function (Eisenstein, 2023)

Given the comprehensive insights provided by the materials in this section, we believe the future directions in clinical brain imaging should emphasize the incorporation of acoustic imaging techniques into existing PA tomographic configurations (Demene et al., 2017; Imbault et al., 2017; Na and Wang, 2021; Na et al., 2022b). This integration provides several advantages, including improved signal discrimination, increased spatial resolution, microvascular-level functional imaging, and drug delivery capabilities. Overall, PA/US holds great promise for revolutionizing clinical brain imaging and advancing diagnosis. Table 4 summarizes the PA and US characteristics for vascular applications.

3.3 Cardiology and endovascular applications

Atherosclerosis, the thickening of the arterial wall caused by the accumulation of cholesterol, lipids, and other constituents, is the leading cause of cardiovascular death and disease. A blockage in blood flow is caused by blood clots formed by vulnerable plaques rupturing from the arterial wall. These plaques are non-obstructive lesions with an elevated risk of breaking down and may cause fatal cardiac events (Richardson et al., 1989; Falk et al., 1995; Schaar et al., 2004; Virmani et al., 2005). Plaque morphology and composition are important diagnostic features for cardiac intervention and

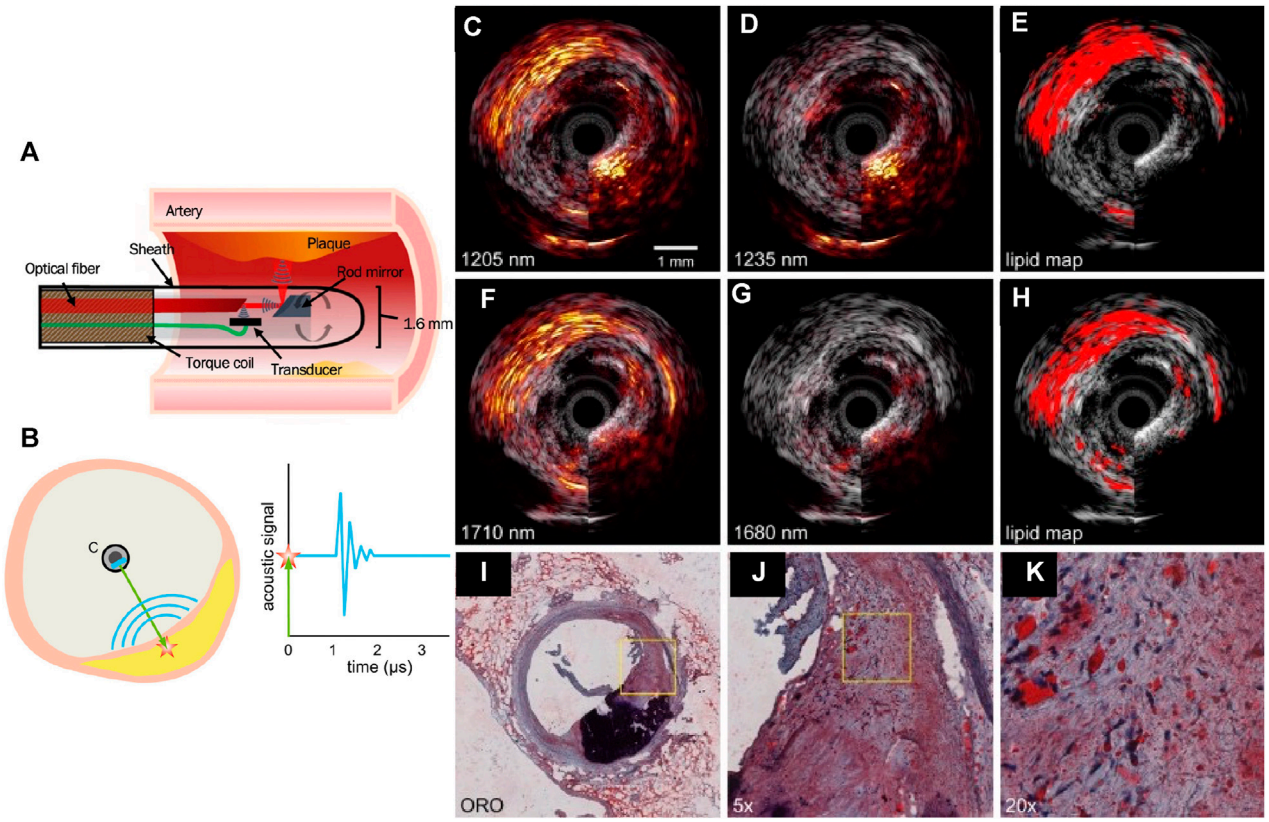

FIGURE 6
(A) A schematic of the IVUS/IVPA collinear catheter design, in which the acoustic and optical paths overlap, after a series of reflections off the rod mirror and optical fiber surfaces. **(B)** Sketch of the intravascular photoacoustic imaging (IVPA) principle. A laser pulse (green) is sent from the catheter C to the vessel wall containing a plaque (yellow). The light excites an acoustic wave (blue curves) through optical absorption and the associated thermoelastic expansion (red star). The graph on the right shows a time trace of the acoustic signal after the laser fires at time t = 0; Lipid detection in an atherosclerotic human coronary artery using sIVPA at 1.2 μm and 1.7 μm. **(C)** 1,205 nm and **(D)** 1,235 nm combined IVUS/IVPA images (IVPA 25 dB, IVUS 40 dB). **(E)** Lipid map based on 2-wavelength relative difference between the PA signal at 1,205 nm and 1,235 nm. **(F)** 1710 nm and **(G)** 1,680 nm combined IVUS/IVPA images (IVPA 25 dB, IVUS 40 dB). **(H)** Lipid map resulting from the 2-wavelength relative difference between the PA signal at 1710 nm and 1,680 nm. Both lipid maps are shown overlaid on the corresponding IVUS image. **(I)** Lipid histology stain (ORO); lipids are stained red; calcification is stained black. **(J)** ×5 magnification of the part of the atherosclerotic plaque indicated as lipid rich by the lipid stains (area outlined in black in (i)), shows larger extracellular lipid droplets, while the lipids in all other parts of the lesion are intracellular or contained in small extracellular droplets. **(K)** ×4 magnification of area outlined in black in **(H)**. Reproduced with permission from (Jansen et al., 2014a; Jansen et al., 2014b; Kole et al., 2019).

subsequent treatment (Kolodgie et al., 2001). Therefore, it is essential to identify and monitor potentially vulnerable areas to prevent and monitor coronary disease progression. Dual-modal intravascular ultrasound (IVUS) and intravascular photoacoustic (IVPA) imaging have made notable contributions to cardiac imaging (Wang et al., 2010a; Karpiouk et al., 2010; Jansen et al., 2014a; Zhang et al., 2014; Hui et al., 2016; van Soest et al., 2017). IVUS/IVPA together is powerful for analyzing atherosclerotic plaques. IVUS differentiates tissues as fibrotic, necrotic, lipidic, and calcified. IVPA provides details of the chemical compositions of vulnerable plaques (see Figures 6A,B) (Wang et al., 2010b; Shin et al., 2011). Advances in transducer design and development are further propelling this dual-modal technique toward smooth clinical translation (Hui et al., 2017; Wu et al., 2017; Cao et al., 2018). In this section, we discuss recent innovations in this field.

3.3.1 Preclinical imaging

IVUS/IVPA was proposed for quantifying perivascular adipose tissue (pVAT), a known symptom of early atherosclerosis (Verhagen and Visseren, 2011; Lee et al., 2013; McKenney-Drake et al., 2017; Tanaka and Sata, 2018), as well as plaque burden for early assessment of the disease. Kole et al., 2019 compared IVUS/IVPA (Figure 6A) with dual-modal near-infrared spectroscopy and IVUS (NIRS/IVUS) (Gardner et al., 2008; Madder et al., 2016; Schuurman et al., 2018) as both NIRS and IVPA are capable of quantifying lipid cores. IVUS/IVPA was able to detect early stages of atherosclerosis in swine *in vivo* based on pVAT, a known cause of atherosclerosis. In terms of depth resolution, IVUS/IVPA outperformed NIRS/IVUS by their ability to localize the lesions. Using IVUS and spectral IVPA at two spectral bands of 1.2 (Figures 6B–E) and 1.7 μm (Figures 6F–H), Jansen *et al.* demonstrated lipid detection and the results match with histology stains (Figures 6I–K) (Jansen et al., 2014b). The results indicate that the 1.2 μm wavelength allows the differentiation of lipids from the arterial wall (Allen and Beard, 2009; Jansen et al., 2011). The 1.7 μm wavelength provides higher sensitivity to lipid absorption with lower pulse energy (Wang et al., 2012). Plaque lipids (cholesterol) and peri-adventitial lipids were differentiated. However, there is a strong calcium absorption signal at both wavelength ranges.

TABLE 5 Obstetrics.

Application	PA characteristics	US characteristics
Obstetrics	Oxygen saturation of hemoglobin (sO_2) for placenta	Blood flow from power Doppler
	Total hemoglobin	Position of placenta
		Embryo size
		Embryo orientation

To obtain multiple lipid components and evaluate lipid concentration, Leng et al., 2021 combined PA/US imaging in a 0.9 mm catheter that performed 360-degree rotation. PA spectroscopy imaging with 11 wavelengths (1,690 nm–1778 nm) was performed. The correlation coefficient was calculated between the experimental PA spectrum and the optical absorption spectrum of lipids to indicate regions of increased lipid deposition. Abran et al., 2014 also designed a PA and US-based catheter, which was also tested for intravascular elastography on phantom.

The limitations of IVUS/IVPA imaging are the slow imaging speeds of −5 frames per second and the lack of real-time capabilities. Hui et al., 2017 addressed this issue by proposing a real-time IVUS/IVPA imaging system with a frame rate of −25 frames per second, comparable to commercial IVUS and NIRS/IVUS systems. This was achieved by utilizing a 2 kHz repetition rate master oscillator power amplifier-pumped OPO (optical parametric oscillator) laser. VanderLaan et al., 2017 also proposed a real-time system with online image processing and display capability of ≥30 Hz frame rates.

IVUS/IVPA technology needs to be thoroughly tested in small-animal atherosclerotic models before moving into clinical space. Along with real-time imaging capabilities, other factors that require improvement are catheter size and the sheath properties. Real-time visualization of the catheter tip is necessary for the operator to identify the correct region of interest. Furthermore, the sheath should be optically and acoustically transparent in the ideal situation.

3.4 Obstetrics

Ultrasound has long been the modality of choice to monitor fetal and maternal health during gestation and detect any complications or developmental defects. However, US alone does not provide functional information, which may be essential (Lawrence et al., 2019). Functional changes in the development of an embryo are essential to understanding developmental abnormalities during pregnancy. Several complications of pregnancy, including genetic defects, preeclampsia, gestational diabetes, or teratogens, can be assessed by studying functional parameters in the conceptus or placental hemoglobin. Furthermore, environmental factors that contribute to toxicity, such as pollution, radiation, and heavy metals, are also leading to an increase in embryonic disorders. These can also be monitored by studying oxygen saturation and hemoglobin concentration. Additionally, more than 50% of congenital heart defects are missed with US imaging (Tegnander and Eik-Nes, 2006; DeVore et al., 2017; Dhillon et al., 2020). Therefore, functional information can be crucial in monitoring both fetal and maternal health during pregnancy. Hence, there is a need to develop imaging methods that are noninvasive and sensitive, as well as provide functional information. Combining PA and US modalities can fill this gap. In this section, recent advances in this field are discussed. Table 5 summarizes the PA and US characteristics for obstetrics.

3.4.1 Preclinical imaging

Preeclampsia, which has led to numerous pregnancy-related deaths, is primarily caused by placental ischemia due to reduced uteroplacental perfusion (Gilbert et al., 2009; Fujii et al., 2017). Placental ischemia is an indicator of preeclamptic risk before the onset of maternal symptoms (Gilbert et al., 2007). Bayer et al., 2017 demonstrated a US-guided spectral PA method for pre-clinical studies of the maternal-fetal environment. Lawrence et al., 2019 demonstrated noninvasive PA/US imaging of a reduced uterine perfusion pressure model (RUPP) to detect placental ischemia (Figures 7A–F). PA images obtained at 690, 808, and 950 nm were obtained and co-registered with B-mode US images. PA/US imaging showed a hypoxic placental environment, which further led to hypertension and proteinuria during late gestation, symptoms for preeclampsia. Arthuis et al., 2017 used PA/US to study the effect of variations in maternal hypoxia in pregnant rats. They found that the placenta is sensitive to oxygen variations. To detect levels of placental oxygenation at different stages of pregnancy, Yamaleyeva *et al.* used PA/US imaging to monitor regional differences in placental sO_2 (Yamaleyeva et al., 2017; Yamaleyeva et al., 2018). PA was used to accurately detect placental sO_2 across various mouse models (ACE2-KO and C57Bl/6). Also, sO_2 at different placental regions (labyrinth and junctional zone plus decidua) through normal and hypertensive gestations was recorded. Due to limited penetration depth (−1 cm), fetal organs were not studied.

Fetal asphyxia, or oxygen deprivation, leads to various health defects such as cerebral palsy, hypoxic-ischemic encephalopathy, and mental impairments (Vannucci, 2000; Sandström et al., 2017). Yan et al., 2021 designed and developed a US, PA, and Doppler endocavity imaging system (ECUSPA) using a commercially available transvaginal ultrasound probe to address fetal asphyxia at birth. Oxygenation maps were obtained from PA (sPA), while structural and blood flow parameters were obtained from US and power Doppler imaging. The system achieved 200 μm spatial resolution at 30 mm depth and a real-time frame rate of 30 Hz. A sO_2 estimation error of less than 10% was evaluated using *ex-vivo* sheep brain and *in vivo* study. While this system can monitor fetal brain blood volume *in vivo* (see Figures 7G,H) and dye distribution *ex vivo* (Figure 7I), the effects of the fetal skull and scalp are yet to be studied.

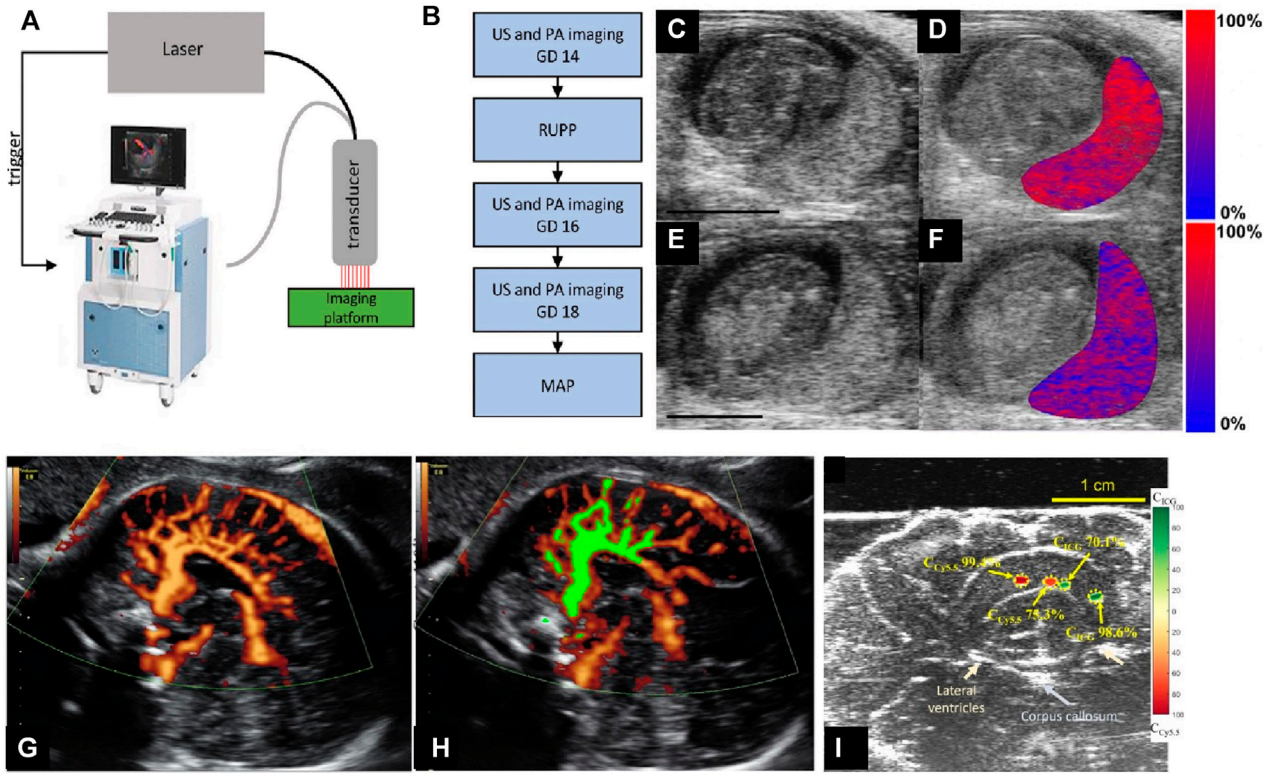

FIGURE 7
(A) The custom-integrated US and photoacoustic imaging system (image of Vevo 2100 reproduced with permission from FUJIFILM VisualSonics). The Phocus Benchtop laser triggers the dual acquisition of US and PA images. Images are acquired using an ultrasound transducer integrated with a fiberoptic bundle for laser light delivery. **(B)** The sequence of the experimental procedures. **(C–F)** B-mode US images of the placental environment of pregnant mice: **(C and E)** show normal pregnant mouse (NP). **(C and D)** shows the reduced uterine pressure model (RUPP). **(E and F)** show mice at gestational day (GD 16). **(D and F)** The oxygen saturation (colormap) of the placental region is segmented and superimposed on the ultrasound image. Red denotes completely oxygenated blood, while blue denotes completely deoxygenated blood. Scale bars are 3 mm. **(G)** Power-Doppler ultrasound (PDU) of cortical arterial and venous blood flow in fetus brain (*in vivo*). **(H)** Normalized FMBV (fractional moving blood volume) image (green mask) overlaid on top of acquired Doppler image, indicating the blood volume is 31%. **(I)** Spectrally unmixed sPA measurements for the relative concentration of ICG and Cy5.5 in excised sheep brain. Color-coded maps indicating the relative concentration of ICG and Cy5.5 and showing the ability of sPA to distinguish and measure the concentration of two spectrally different absorbers. Reproduced with permission from (Lawrence et al., 2019; Yan et al., 2021).

To investigate the effect of heavy metal toxicity on fetal development, Qiu et al., 2022 used PA and US tomography to detect developmental toxicity in fetuses exposed to Methylmercury Chloride (MMC). Mice embryos at different stages of development were studied. Various parameters, such as US and PA signal intensity, oxygen saturation, total hemoglobin content for the heart, and PA signal ratio of the embryonic heart and amniotic fluid, were recorded. PA/US imaging was able to detect changes in these parameters *in utero*. While these results promise the detection of aberrant embryonic development, further studies with larger sample sizes and different toxicity models need to be conducted.

Placental insufficiency can lead to numerous complications, such as preeclampsia, fetal growth restriction, gestational diabetes, spontaneous preterm birth, and even pregnancy loss. Therefore, studying functional changes in the placenta is essential (Wu and Bayer, 2018). While the above-mentioned studies have shown that a hypoxic placental environment leads to preeclampsia, additional preclinical studies are necessary to thoroughly understand the functional characteristics of the placenta along with its role in other pregnancy-related issues.

3.5 Joint imaging

Joint disorder refers to a set of chronic arthritic conditions associated with considerable pain, mobility impairment, and reduced quality of life. Among joint diseases, rheumatoid arthritis (RA) and osteoarthritis are the two representative arthritis diseases, with osteoarthritis being the most common form of arthritis (Barbour et al., 2017), and arthritis being the leading cause of disability in the last 15 years (Yelin et al., 2016). The adaptation of high-frequency gray-scale B-mode in conjunction with power Doppler allows visualization of anatomic structures and abnormal blood flow toward arthritis diagnosis (Schmidt, 2007). However, due to the principle of Doppler imaging, the US-PD system is angle-dependent and more sensitive to fast blood flow in relatively large vessels, whereas blood flow in smaller capillaries has a closer correlation with early arthritis symptoms (Goldie, 1969). PA/US thus has been studied as a complement to US-PD for imaging small vessels. Table 6 summarizes the PA and US characteristics for joint imaging.

TABLE 6 Joint imaging.

Application	PA characteristics	US characteristics
Joint	Neovascularization in the TTF region	Low echo area generated in the TTF region
	Synovium hyperemia	Synovium boundary delineated by bones and tendon
	Nailfold capillary	Skin thickness between the nail fold and the distal interphalangeal joint
	Oxygen saturation in the nailbed	Cross-sectional tendon, bone, tissue surface, aponeurosis
	Cross-sectional vascular structures, skin surface layer, epidermal-dermal junction	

3.5.1 Preclinical imaging

Wang et al. proposed a microscopic-based PA/US system for joint evaluation. The system used a 532 nm laser wavelength and a central frequency of 25 MHz to image the mouse knee joint (Wang et al., 2023a). The results of coaxial dual-modal imaging showed that the US can effectively visualize the synovial erosion area as a hypoechoic region within the tibiofemoral tendon-tibia-femur (TTF) complex. On the other side, the PA signal generated in the same region can be correlated with the grades of Rheumatoid Arthritis (RA).

Despite a relatively rapid scanning speed of 10 mm/s, one of the limitations of this system is its limited penetration depth (1.5–2.1 mm) compared to other configurations. Moreover, factors such as the cost and ease of use hinder the widespread clinical utility and acceptance of PA/US microscopy. As a result, the application of PA/US microscopy for joint evaluation is restricted to mouse models. In contrast, PAT configuration has gained prominence in clinical research due to its superior penetration depth. The following section covers the ongoing exploration of human joint experiments utilizing dual-modal tomographic platforms.

3.5.2 Clinical imaging

Based on the system configurations, joint imaging setups using PA/US tomography can be divided into linear arrays (Xu et al., 2013; Daoudi et al., 2014; Yuan et al., 2014; Jo et al., 2017; Daoudi et al., 2021) and ring arrays (Mercep et al., 2015; van Es et al., 2015; Liu et al., 2016; Oeri et al., 2017). Linear array configurations perform joint evaluation by placing the hand-hold transducer in direct contact with the skin over the targeting area (Figure 8A) (Daoudi et al., 2014). Linear arrays offer a comprehensive visualization of the joint, including the skin, blood vessels, tendons, and underlying bone (Figure 8B). The clinical experiment verified that the acquired PA signal around the US-acquired phalanges structure can be used for assessing inflammation-induced hyperemia (Jo et al., 2017). A later study adapted a central frequency of 21 MHz for PA to visualize capillaries and a frequency of 40 MHz for the US to track sub-millimeter skin thickness in superficial regions (Oh et al., 2006). The resulting multi-spectral PA/US images provide accurate quantification of the target joint, including capillary density (PA), skin thickness (ultrasound), and oxygen saturation inside the nail region. These findings stated the potential of using specific central frequencies to target distinct features. Additionally, real-time dual-modal imaging has been successfully achieved by employing a specially designed GPU-compatible back-projection algorithm (Wang et al., 2016).

One limitation of the linear transducer is the limited view angle. Cross-sectional ring-shaped configurations have been investigated to address this issue (Mercep et al., 2015; van Es et al., 2015; Liu et al., 2016; Oeri et al., 2017; Guo et al., 2019) (Figure 8C). For cross-sectional imaging, the finger was placed at the center of the ring-shaped transducer array and immersed into the water tank. Ring arrays generate images that cover the full cross-sectional depth of the joint. With hardware advancements (Oeri et al., 2017) and improved reconstruction methodologies (Mercep et al., 2015), Oeri et al. (Oeri et al., 2017) achieved real-time finger imaging with full-angle coverage. The array can further move along the finger for volumetric imaging. Stacking images along the scanning direction yields a volumetric imaging window of $20 \times 20 \times 20\ mm^3$, with isotropic in-plane image resolutions of 150 μm and 160 μm for PA and US, respectively. Figure 8D shows coronal and axial images of the figure acquired by such a system. The cross-sectional PA/US image reveals the finger tendon, bone, tissue surface, upper aponeurosis, and finger vasculature structures. These characteristics can indicate rheumatoid arthritis symptoms such as edema, joint effusion, and bone erosions for joint diagnosis (van Es et al., 2015).

Another method to achieve ring-shaped imaging is to employ a beam splitter in conjunction with numerous fibers to evenly split the emitted laser beam at 360° and conduct illumination (Liu et al., 2016; Guo et al., 2019). The PA image area can be used to estimate corresponding joint size and angiogenesis to supplement the US anatomic information for joint evaluation. The human experiment validated the system's ability to track rheumatoid arthritis progression and recovery. However, the system's resolution of 80 and 600 μm along lateral and axial directions prevent the differentiation of small vessels and capillaries in the cross-section images (Guo et al., 2019).

Researchers have also investigated the performance of functional PA/US for joint evaluation. Previous preclinical studies have shown that biomarkers, including hyperemia location, hypoxia in synovial tissue, and the number of high amplitude PA pixels could be used to diagnose joint disease (Jo et al., 2017; van den Berg et al., 2017). Zhao et al. developed a dual-modal system diagnosis protocol that integrates those factors into a novel parameter named PA + sO_2 pattern, and the combined parameter's performance was validated in human experiments (Zhao et al., 2021a). The proposed parameter was compared against standard clinical scores, including the simplified disease activity index (SDAI), clinical disease activity index (CDAI), and the disease activity score, in 28 joints (DAS28). Statistical analysis reveals that the PA + sO_2 pattern is highly correlated with those parameters of the targeted joint and

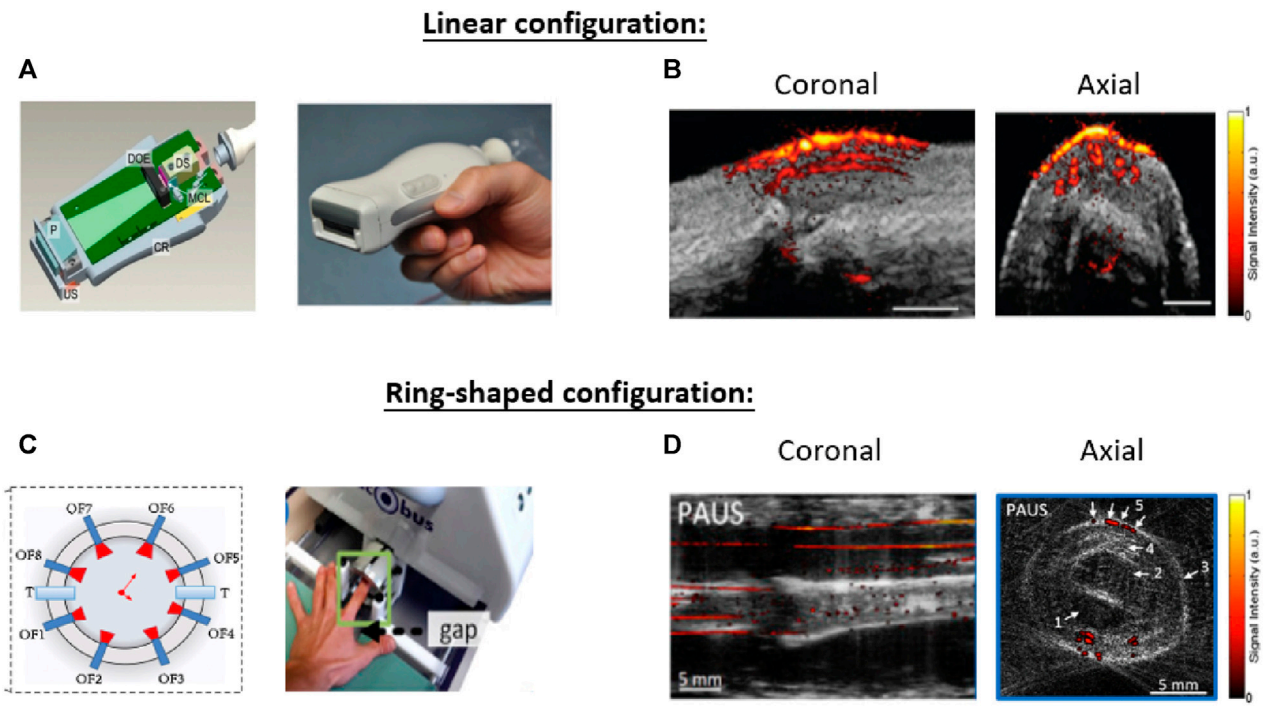

FIGURE 8
Two kinds of system configurations that have been investigated for PA/US joint imaging. **(A)** The combination of a light source and linear US array can obtain cross-sectional images of the target joint **(B)** The overlapped PA/US image contents anatomic and functional information to detect diseases. **(C)** A segmented full-ring-shaped transducer captures the target finger with the finger being placed in the center of the transducer. **(D)** Arrows 1-4 in the axial image highlight the anatomical structures provided by the US and arrow 5 highlights the microvasculature structure provided by PA. The finger structure along the coronal direction was formed by stacking the axial slices along the scanning direction. Reproduced with permission from (Daoudi et al., 2014; Jo et al., 2017; Oeri et al., 2017).

outperforms the traditional power Doppler in certain joints due to its greater sensitivity to small vessels. Assessing sO_2 concentration can also help with patient treatment because hypoxia is associated with higher visual analog scale (VAS) and patient's global activity (PGA) scores.

The application of PA/US in joint evaluation has been extensively studied with various configurations. While circular scanning configurations generally outperform linear arrays in terms of imaging angle and penetration depth, the implementation of this approach in clinical practice is hindered by the impracticality of the bulky water tank. In contrast, linear transducers offer advantages for clinical translation due to their compatibility with existing commercial ultrasound imaging units. The penetration depth is the major limit of linear configurations that hindered its applications. Clinical research on linear arrays has primarily focused on finger evaluation, with limited exploration of larger joints. Toward this issue, Jo et al. stated in their study that a wavelength around 580 nm is adequate for PA diagnosis of human hand joints, and wavelengths in the optical spectrum of 650–950 nm are theoretically sufficient for larger joints such as the ankle (Xu et al., 2013). Further research is necessary to provide experimental support toward this expectation. Another potential solution worth exploring involves the rotation of the transducer. The study proposed by Francis et al. demonstrated a linear configuration by rotating the linear transducer and employing repeated side illumination with a calculated number of angular views to achieve full-view tomographic imaging (Francis et al., 2020). This innovative approach holds promise for achieving significant penetration depth within a clinical setting using a linear setup.

Finally, achieving higher imaging quality is paramount for PA/US to potentially replace well-established clinical imaging methods such as MRI (Zhao et al., 2021b). There is existing research that holds promise for future implementation in PA/US. In terms of hardware, the use of LEDs as the PA light source has been investigated as a means to identify inflammatory arthritis with increased system portability (Jo et al., 2021). As for image reconstruction, efforts are made to improve image quality by mitigating artifacts stemming from acoustic reflection by bone surfaces (Biswas et al., 2015) or by estimating the initial pressure distribution and speed-of-sound distribution (Matthews and Anastasio, 2017a). It is necessary to explore the performance of both reconstruction algorithms in patient imaging with PA/US, as it may prove critical for the clinical advancement of the PA/US modality.

3.6 Dermatology

While skin diseases are often overlooked in terms of health priorities, they affect 27% of the population in the US (Barbour et al., 2017) and are the fourth leading cause of non-fatal disability (Seth et al., 2017). The most common method for skin diagnosis is a skin biopsy. However, due to its limited field of view, reliance on lesion age, and invasive nature, alternative approaches are actively explored (Li et al., 2021). PA/US has the potential to meet this clinical need. Table 7 summarizes the PA and US characteristics for skin imaging.

TABLE 7 Dermatology.

Application	PA characteristics	US characteristics
Dermatology	NPs accumulated in the melanoma	Gas bubbles generated in the melanoma
	Feeding vessels extend from the melanoma	Normal tissue surrounding the melanoma
	Melanin distribution	Melanoma contour
	CTC concentration	Depth extension of melanoma
	Content of melanin in each CTC	Structural information of the target veins for CTC tracking (size, depth, flow velocity, etc.)
	The moving speed of CTC	

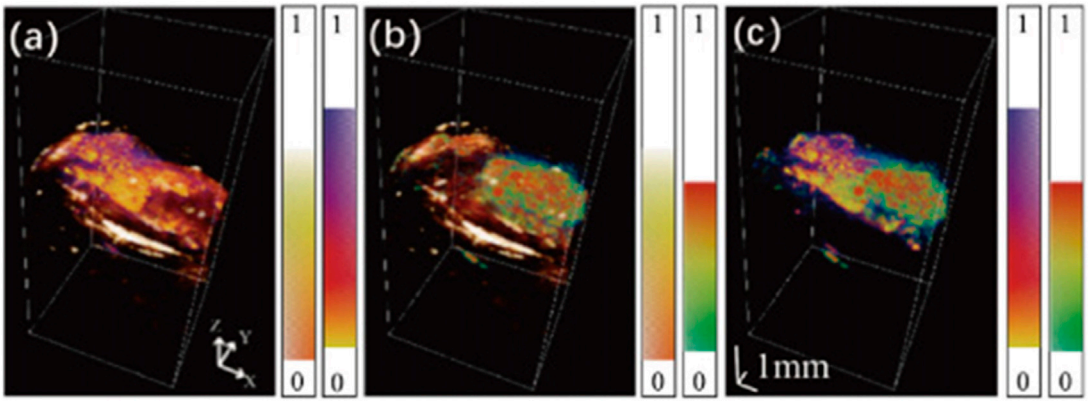

FIGURE 9
Fused image between **(A)** Visible light PA image and US image, **(B)** NIR light PA image and US image, and **(C)** Visible light PA image and NIR light image. Each imaging modality reveals different information about the target tissue, which allows a more comprehensive evaluation of melanoma through cross-correlation. Reproduced with permission from (Wang et al., 2021) © Optical Society of America.

3.6.1 Preclinical imaging

Melanoma is the most dangerous type of skin cancer, and sonography can be used to diagnose skin cancer by measuring tumor-induced melanoma thickening (Pellacani et al., 2005; Scotto di Santolo et al., 2015). However, because of the low contrast in the superficial region, this method shows poor accuracy in early-stage melanoma (Swetter, 2003). On the other hand, while PA is effective at characterizing superficial vasculature changes (Oh et al., 2006), it is incapable of deep penetration due to high light attenuation. To overcome the limitations of stand-alone imaging modality, multiple PA/US preclinical models have been proposed for a comprehensive diagnosis of melanoma by monitoring different tumor features (Wang et al., 2016; Wang et al., 2021). Microscopic PA/US imaging is well suited for small animal imaging as it offers high spatial resolution. As shown in Figure 9, the fused PA image obtained with visible and NIR light gives accurate volumetric mapping toward the melanoma entity and surrounding tissue, and the US allows more accurate localization of tissue boundaries. Moreover, the near-infrared light increased the penetration depth of PA to 8mm, which facilitates the correlation between PA and US modalities for more precise volumetric localization of the melanin boundary (Wang et al., 2021). Despite all these advantages, the acquisition time required by existing configurations lasts from several minutes (Wang et al., 2016) to close to an hour (Wang et al., 2021). As a result, the application of PAM for melanoma diagnosis remains in animal models so far.

On the other hand, researchers also constructed novel contrast agents that improve the PA/US signal for melanoma imaging (Li et al., 2018). The melanoma-targeting nanoprobe is encapsulated in liquid perfluorohexane, a substance that can be vaporized and transformed from droplets to microbubbles via optical irradiation. The nanoprobe is applied to the tumor-bearing mouse, followed by dual-modal transducer imaging with a central frequency of 21 MHz. The team revealed a progressive increase in PA and US signals due to the applied nanoprobe and the micro-bubbles generated from the light-excited nanoprobe. Thus, they verified the nanoprobe's capability to enhance the contrasts between tumor-induced vessel structures and corresponding anatomical structures.

3.6.2 Clinical imaging

As stated in the preclinical section, the existing microscopic-based PA/US system for skin diagnosis is limited by the acquisition time and unsuitable for clinical imaging. So, in human imaging studies, linear-array-based PA/US systems are used to increase imaging speed (Breathnach et al., 2015a; Breathnach et al., 2018; Park et al., 2021a). Combining PA and US modalities enables comprehensive diagnosis of melanoma. As shown in Figure 10,

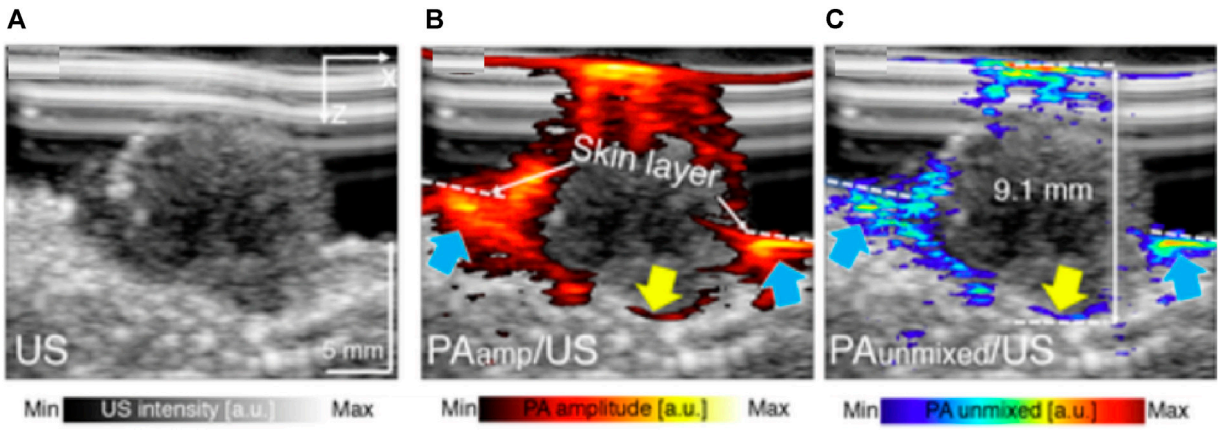

FIGURE 10
PA/US melanoma entity imaging results. **(A)** The B-mode US imaging result of a nodular type of melanoma **(B)** The PA amplitude and **(C)** spectrally unmixed PA images are overlapped to the US image to provide corresponding functional information. The blue arrows indicate the location of invasive sites marked by feeding vessels, and the yellow arrow marked the bottom boundary of the melanoma. Reproduced with permission from (Breathnach et al., 2015b).

PA image reveals the feeding vessels, while US assesses the tumor extension in the depth direction. Furthermore, one of the studies confirms that melanoma-generated PA signals mainly came from wavelengths of 800 and 1,064 nm, while signals generated from the interface between melanoma and normal tissue mainly came from 680 nm excitation (Zhao et al., 2021a). Taking advantage of this characteristic, spectrally unmixed PA gives a precise measurement of the shape and location of the melanoma (Figure 10C). Combining the structural and functional information facilitates more accurate surgical excision targeting different stages of the disease. Furthermore, the research proposed by Park et al. (Park et al., 2021a) achieved a penetration depth of 9 mm so that it is possible to analyze the boundary architecture of the melanoma entity and correlate it with the sub-type of melanoma.

Aside from imaging the melanoma entity, the PA/US modality is also studied as an alternative approach to tracking melanoma metastasizes in regional lymph nodes. Clinical experiment (Dean-Ben and Razansky, 2021) has verified the PA/US configuration's potential to replace the conventional radioactive lymphoscintigraphic imaging approach (Stoffels et al., 2019). A following study proposed by Stoffels et al. shows that PA/US can achieve comparable melanoma metastasizes detection against the lymphoscintigraphic, which is the clinical gold standard, with a maximum penetration depth of 5 cm (Stoffels et al., 2015). The imaging results obtained from 20 patients reveal a system *in vivo* sensitivity of 100%, which outperformed the traditional lymphoscintigraphic, and the anatomic information provided by the US also paved the way for PA/US-guided minimally invasive surgery in the future. Due to the high false positive rate caused by the presence of other optical absorbers in the tissue, the team reported the system specificity to be 48.6%. However, the team believes incorporating a contrast agent could potentially solve this problem in the future.

Also aiming to assist melanoma diagnosis, Galanzha et al., 2019 proposed a novel approach utilizing PA technology to detect circulating tumor cells (CTCs) disseminating from the primary tumor into the bloodstream, which can lead to early metastases and blood clot formation. The team used the PA modality to visualize the cell in conjunction with the vessel structure provided by the US to anatomically localize the CTCs. Experiment results revealed the relationship between the CTCs flowing velocity and position within the vessels. However, the examination of the approach varies from 10 to 20 s to 1 h for patients with different CTCs concentrations, making it unsuitable for individuals with a lower CT concentration.

Finally, one non-cancer-related PA/US clinical skin imaging used PAM and high-frequency ultrasound to characterize skin aging, featured with increased skin vessels (Saijo et al., 2019). The team has confirmed that the system can achieve a spatial resolution of 24 × 16 μm in horizontal and axial directions, with a penetration depth of 2 mm to visualize superficial microvascular structures and oxygen saturation status with the multi-spectral PA modality. The US modality, on the other hand, can provide the corresponding tissue structures across the dermis layer.

3.7 Dental applications

Oral diseases pose a significant global public health challenge due to their widespread occurrence, negative impact on the quality of life, and the considerable resources needed for treatment (Sheiham, 2005). Among the oral conditions that affect both the hard and soft tissues of the oral cavity, periodontal disease, tooth decay, and oral cancer are the most prevalent (Feldchtein et al., 1998). Despite more than 60% of adults regularly undergoing dental evaluations each year, current imaging methods have certain limitations when it comes to the early detection of oral diseases (O Connor et al., 2015). Previous research has indicated that for existing imaging modalities, CT has limited precision, MRI lacks sufficient spatial resolution, wide-field autofluorescence imaging suffers from low diagnostic specificity, and dental X-ray exposes patients to ionizing radiation (Pierce et al., 2012; Sarrion Perez et al., 2015; Hwang et al., 2018). Recognizing the necessity to evaluate

TABLE 8 Dental.

Application	PA characteristics	US characteristics
Dental	Tongue vessel (clusters for small ones)	Internal structure of the tongue
	Contrast agent labeled pocket, gingiva and occlusal surface	Periodontal structure (gingiva, occlusal surface, pocket, etc.)
	Embedded implant	Structure/thickness of the soft tissue surrounding the implant

features from various hard and soft tissues, several dual-modal imaging approaches have been developed to enhance the diagnostic accuracy of oral diseases (Hucker et al., 2008; Niedre and Ntziachristos, 2008; Kalchenko et al., 2011; Nam et al., 2012; Lee et al., 2018). One such approach is the utilization of the dual-modal PA/US, which is concluded in this section. Table 8 summarizes the PA and US characteristics for dental imaging.

3.7.1 Preclinical imaging

PA/US has been investigated for clinical dental implant testing (Lee et al., 2018). The team imaged a dental implant-anchored porcine jawbone wrapped in 1 cm thick chicken breast. The results verified the ability of the PA/US modality to penetrate through the covered tissue and produce co-registered volumetric images of soft tissue, jawbone position, and implant site, as shown in Figure 11 (Lee et al., 2017). This approach can potentially help dentists plan and execute implant treatments more effectively in dental clinics.

The integration of Fluorescence Lifetime Imaging Microscopy (FLIM) configuration toward PA/US modality has been investigated by Fatakdawala et al. for carcinoma diagnosis (Fatakdawala et al., 2013a). The tri-modal system incorporated a ring ultrasonic transducer attached to 16 optical fibers for the PA/US subsystem and another fiber bundle extended from the middle for the co-registered FLIM imaging. The team examined the performance of the system with twenty-four male, golden/Syrian hamsters. The FLIM provides metabolic information by differentiating normal tissue from cancerous tissue based on differences in fluorescence signatures owing to changes in collagen content. This innovative tri-modal design offers the potential to identify regions of high metabolic activity in tumors using FLIM and further characterize these regions using PA and US to assess blood vessel density and structural changes in the surrounding tissue, thereby providing a comprehensive assessment of tissue structure and function.

3.7.2 Clinical imaging

While the previously proposed dual-modal imaging configuration is too bulky (Fatakdawala et al., 2013a), Guo et al., 2018 construct a compact transducer probe for dual-modal carcinoma diagnosis inside the human oral cavity. The team condensed a 2 mm optical bundle and a focused transducer into a side-view probe with a diameter of 14.7 mm. Figure 12A depicts the system's construction along with the acquired PA/US images. During imaging, the probe was attached to a motorized rotator and employed within the oral cavity, performing 360 A-line scanning to cover a 270-degree field of view (FoV) with a step size of 250 μm. Human imaging outcomes revealed that the configuration could generate 3D images of vasculature and tongue structures with a penetration depth of 5.5 mm, allowing tumor detection in the flattened tongue. However, the calculated spatial resolution of the system was limited to 420 and 340 μm for the PA and US modalities, which makes distinguishing smaller vessels challenging.

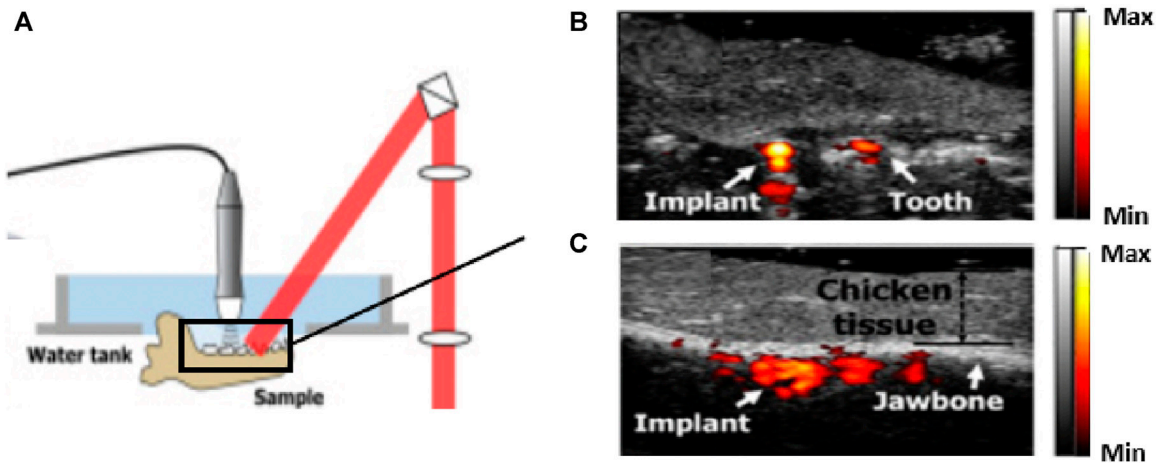

FIGURE 11
Preclinical study for PA/US dental implant imaging. **(A)** The system is utilized for dental implant assessment. **(B)** and **(C)** The cross-sectional dual-model imaging results. The team covered 10 mm thick chicken breast tissue on the target jawbone. Structures (implant, teeth, and jawbone) can be visualized with the PA signal to identify the location of the implant. This result suggests the potential of the PA/US technique to be used for implant treatment, such as to guide needles and drills. Reproduced with permission from (Lee et al., 2017). © Optical Society of America.

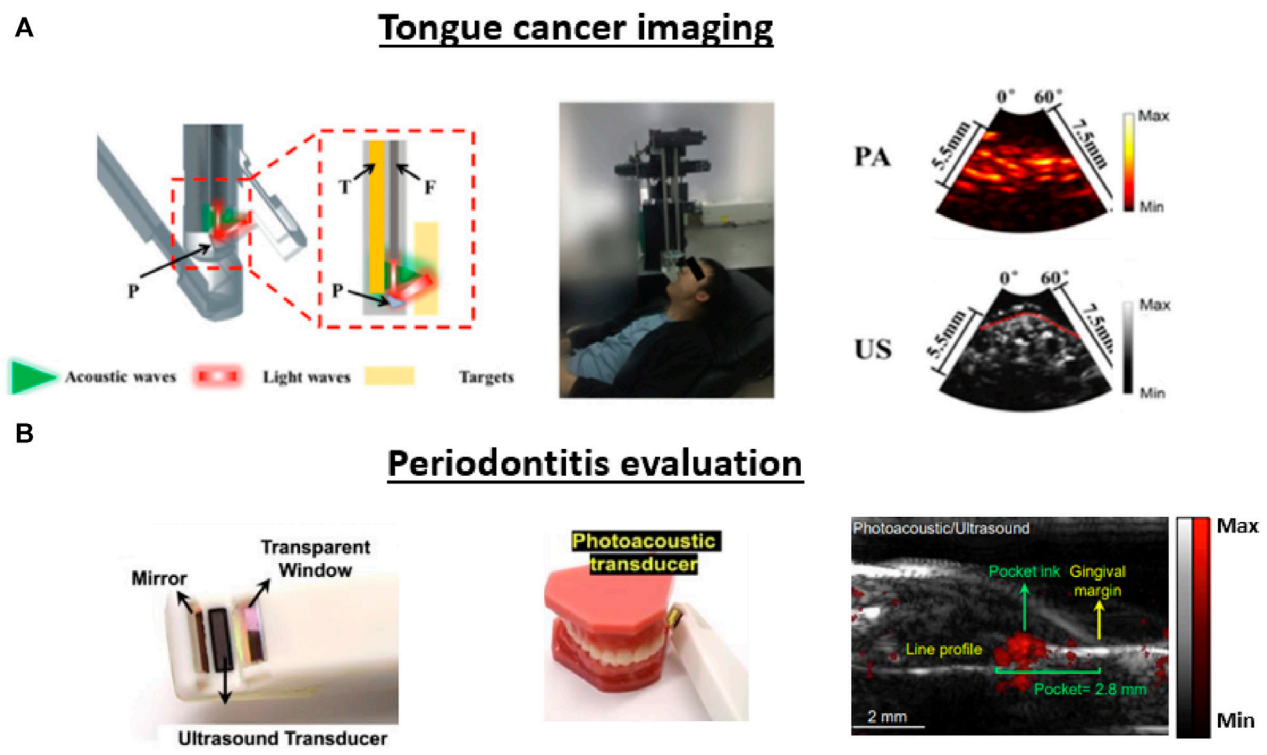

FIGURE 12
Different applications of translational PA/US oral imaging. **(A)** and **(B)** present the system configuration, image acquisition procedure, and PA/US image outputs for studies mentioned in this section. **(A)** Dual-modal imaging system used for carcinoma imaging. A motorized rotator is integrated into a focused transducer to conduct PA/US imaging inside the oral cavity. **H**: resinous holder, T: Transducer, **F**: Fiber bundle, P: Prism. Both generated images contained a 60-degree FoV, and the red dashed line symbolized the surface of the tongue. **(B)** The specially designed hand-hold probe with a small tip in the front facilitates full-mouth scanning. The system can conduct pocket depth measurements with a contrast agent applied to generate PA signals in the pocket. Reproduced with permission from (Khan and Cabanilla, 2009; Moore et al., 2018).

In addition to its applications in oral cancer imaging, the PA/US modality has also been investigated for periodontal applications. The current methods used to evaluate periodontitis often involve invasive imaging of pocket depth using a metallic probe to evaluate the destruction of the supporting structures of the teeth (Khan and Cabanilla, 2009). Given that deeper periodontal probing depths and gingival inflammation are the most common biomarkers of the disease, PA/US is investigated as a potential non-invasive approach. To address the lack of blood supply in the periodontal site, Fu et al., 2022 explored the usage of a contrast agent derived from cuttlefish ink to distinguish the periodontal site from the surrounding soft tissue for functional imaging. The feasibility of this contrast agent was verified in human teeth located at the distobuccal, mesiobuccal, and buccal sites (Moore et al., 2018). Subsequently, the team constructed a toothbrush-shaped compact probe with a central frequency of 19 MHz to achieve full-mouth coverage, including the posterior teeth (Khan and Cabanilla, 2009). To mitigate motion artifacts caused by the handheld configuration, the researchers also devised a modality-independent neighborhood descriptor (MIND)-based image registration technique, reducing motion-induced errors by a factor of ten (Mozaffarzadeh et al., 2021). Patient imaging studies showed that the PA/US images can reveal full-pocket geometry with co-registered anatomic information (Figure 12B). The contrast agent provides an SNR higher than 10 dB at 11 mm, which is more than sufficient for periodontal pockets (typically around 4 mm in depth). The PA/US method can predict gingival inflammation by exploiting the PA signal intensity, and the comparison between the US image and the conventional invasive methodology demonstrates good agreement (less than 7% difference).

PA/US oral imaging has been investigated for different applications in preclinical and clinical studies. The studies covered in the preclinical section are still in the early stages but hold great potential for clinical studies in the future. For implant examination, further investigation is necessary to evaluate implant integration and peri-implant bone health and perform longitudinal monitoring of implant stability. Such advancements can enhance the success rates of dental implant procedures and facilitate long-term monitoring of implant stability, contributing to improved clinical outcomes. Integrating PA/US with other imaging modalities, such as FLIM in oral imaging, expands the capabilities of the system, enabling a more comprehensive assessment of oral tissues. The combination of metabolic, vascular, and structural information provides a holistic view of the pathology, offering the potential for more accurate diagnoses and individualized treatment, ultimately leading to better patient outcomes. Continued research and development in integrating PA/US with other modalities will drive advancements for PA/US oral imaging and its clinical applications.

TABLE 9 Foot ulcer imaging.

Application	PA characteristics	US characteristics
Foot Ulcer Imaging	Oxygen saturation of hemoglobin (sO2) post occlusion	Foot contour
	Vascular structure	Bone structure

We believe there's more potential in the PA/US modality for oral diagnosis. In the current PA/US applications for oral imaging, single-wavelength imaging restricts the system's capability. There is a need to explore multi-spectral imaging for functional oral diagnosis. Evaluating parameters such as blood flow and oxygenation levels can offer valuable information, leading to a more comprehensive understanding of oral pathologies and potentially improved diagnosis of oral diseases. Additionally, while existing research has demonstrated the advantages of microscopy and tomography-based PA in detecting and characterizing early-stage oral pathologies, none of these studies have extended to dual-modal configurations (Li and Dewhurst, 2016; Zhang and Wang, 2022). Integrating the PA system with ultrasonic modality can potentially enhance the identification of subtle abnormalities and lesions in the early stages, providing a more effective diagnostic approach.

3.8 Foot ulcer imaging

Millions of Americans are affected by peripheral vascular disorders associated with pain, functional impairment, amputation, and higher risk of death (Nelson et al., 2007; Sen et al., 2009; Boyko et al., 2018). In addition, diabetes affects the entire vascular system due to long duration of high blood glucose levels, which causes changes in blood viscosity and arterial wall tension. Also, a hyperglycemic state causes altered metabolism, which further leads to altered vascular function at the tissue and cellular level (Pinhas-Hamiel and Zeitler, 2005; Shrikhande and McKinsey, 2012; Cho et al., 2018). Therefore, patients with diabetes are at increased risk of vascular damage and diabetic foot ulcers. Treatment involves revascularizing the limb surgically in order to restore blood flow and perfusion (Ma et al., 2019). Thus, foot perfusion monitoring pre- and post-sugery is necessary to effectively assess the treatment outcome (Huang et al., 2023). Dual-modal PA/US systems are well suited for this application as external contrast is not needed (Wang and Hu, 2012; Choi et al., 2018). Table 9 summarizes the PA and US characteristics for foot imaging.

3.8.1 Clinical imaging

Using a PA/US real-time foot imaging system with an arc-shaped transducer array, Yang et al., 2020 compared diabetes mellitus patients to healthy volunteers. The PA signal intensity and oxygen saturation (sO_2) were compared with and without vascular occlusion in both groups. Doppler US was used to establish landmarks and regions of interest. PA images were acquired at 760 and 840 nm before occlusion and at 800 nm during vascular stimulation. In diabetic patients, after vascular occlusion, slow recovery of PA signal was observed in the arteries. Thus, researchers found that diabetic patients had a unique peripheral hemodynamic response and a lower sO_2 in comparison to healthy subjects. However, this system imaged only cross sections of the foot.

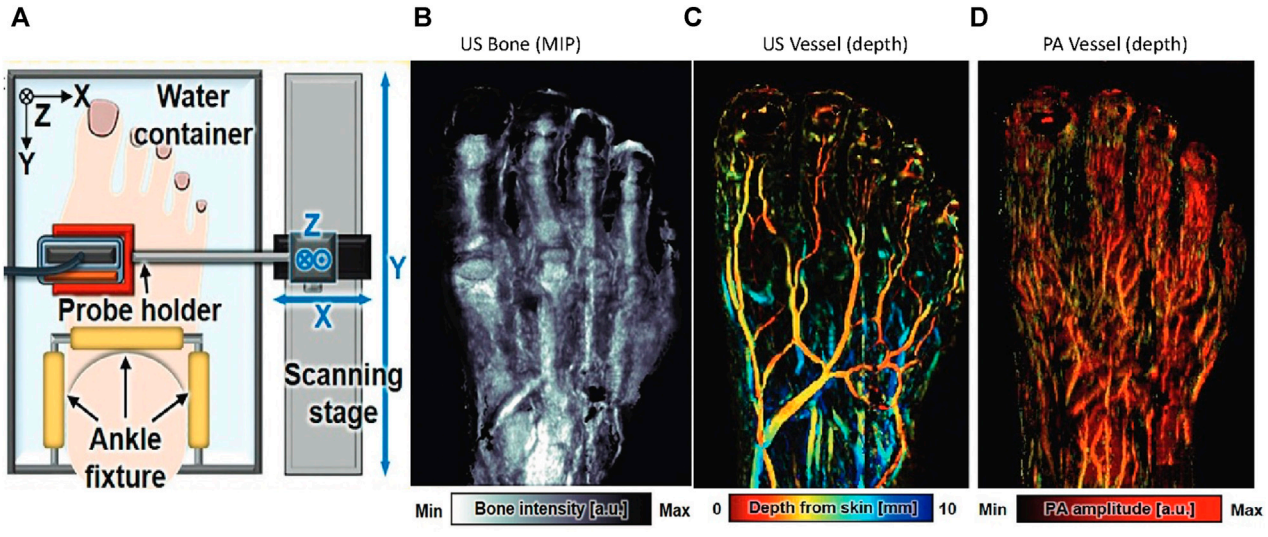

FIGURE 13
(A) Schematic of the 3D PA/US bimodal foot scanning system. Multispectral noncontrast PA/US images obtained from a healthy 32-year-old male volunteer's foot. **(B)** US maximum intensity projection (MIP) bone image. **(C)** US vessel image. **(D)** PA vessel image. a.u. = arbitrary units, max = maximum, min = minimum. Reproduced with permission from (Choi et al., 2022).

TABLE 10 Stem cell therapy.

Application	PA characteristics	US characteristics
Stem cell therapy	Nano tracer for the stem cell	Tissue structure of the imaging site
	Subcutaneous bleeding levels	Morphological changes during wound closure
	Re-establishment of blood perfusion	The entity of the implanted scaffold
	Re-endothelialization of the scaffold	
	Needle guidance for cell delivery	

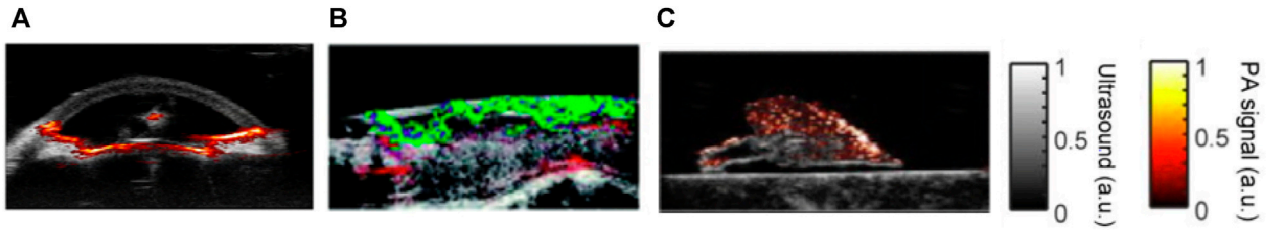

FIGURE 14
Various applications of dual-modal PA/US in combination with contrast agents to track stem cells. **(A)** The anterior chamber of the eye, with the US to visualize the trabecular meshwork and PA to visualize the circulation of the injected stem cells. **(B)** Cross-sectional wound bed with stem cells marked in green and new-grown microvasculature structures in red. The US modal can visualize the wound closure procedure. **(C)** Re-endothelialization of lung scaffold. The US shows the scaffold entity, and the overlapped PA can monitor the stem cell distribution over the scaffold to monitor the capillary formations. Reproduced with permission from (Sun et al., 2012; Nam et al., 2015; Nagao et al., 2016; Kubelick et al., 2019).

To detect microvascular changes in the healthy foot with occlusion, Choi et al., 2022 developed a 3D PA/US foot imaging system (Figure 13A). The contour of the foot was mapped by scanning the foot with US, and then a refined scanning along the mapped contour was performed in both PA and US. As shown in Figures 13B–D, the US modality provides bone and macrovascular information, while the PA modality provides microvascular information. Images from the two modalities were merged to provide 3D morphologic information about the foot. The current setup requires the foot to be completely immersed in water, which may be inadvisable for patients with wounds.

3.9 Stem cell therapy

Stem cells have gained significant recognition in tissue engineering as a cell source capable of replacing or enhancing tissue functions through their remarkable capacity for differentiation into specialized cell types (Li and Dewhurst, 2016). PA/US imaging has emerged as a valuable tool for monitoring stem cells. By combining PA mapping of stem cell distribution with anatomical information obtained through ultrasound, stem cells can be visualized and accurately tracked. This integrated approach enables researchers to monitor the migration, homing, and engraftment of stem cells, thereby contributing to the advancement of effective stem cell-based therapies. This section provides a comprehensive overview of various PA/US applications related to stem cells. Table 10 summarizes the PA and US characteristics for stem cell imaging.

3.9.1 Preclinical imaging

Stem cells lack the optical absorption required for PA visualization. As a result, contrast agents are prevalently used to label stem cells for targeted PA imaging (Ricles et al., 2011; Chung et al., 2013). Various studies have reported the application of gold nanoparticles in tissue engineering as the contrast agent due to their biostability and non-toxicity (Nam et al., 2015; Nagao et al., 2016; Kubelick et al., 2019; Mohd-Zahid et al., 2020). Aside from that, another type of nanoparticle named Prussian blue nanocubes (PBNCs) is applied in a tri-model study for spinal cord therapy (Kubelick and Emelianov, 2020a; Kubelick and Emelianov, 2020b).

As shown in Figure 14, the nanoparticle-aided PA/US modality utilized US to offer structural information of the target region and PA to monitor the injected stem cell via the nanoparticle signal. Mouse experiment quantified the lowest detectable stem cell concentration to be 1×10^4 cells/mL for the nanoparticle-aided PA modality (Nam et al., 2012), which is superior to other noninvasive stem cell tracking methods (Li et al., 2010). High-frequency (20–40 MHz) tomography-based multi-spectral PA/US configuration has been studied as a longitudinal stem cell monitoring platform for various applications. Existing research has demonstrated the capability of the system in visualizing stem cell delivery in the anterior eye (Figure 14A) (Lee et al., 2018), stem cell-mediated wound healing progress (Figure 14B) (Nam et al., 2015), and cell distribution in the acellular scaffold (Figure 14C) (Nagao et al., 2016). Imaging results show that the PA/US offers a favorable balance between penetration depth (several centimeters) and spatial resolution (at the micron level). Multi-spectral imaging enables researchers to separate the signal produced by nanoparticles

from other naturally occurring compounds, such as hemoglobin or melanin to provide functional information (Nam et al., 2015; Kubelick et al., 2019).

Aside from stem cell monitoring, another application of PA/US modality is guided-needle placement for direct stem cell injection. This approach has been used for real-time stem cell delivery to the spinal cord by mounting the PA/US transducer to the spinal injection platform to visualize the needle orientation and the labeled stem cells simultaneously (Donnelly et al., 2018). The team stated that this method can more effectively ensure the proper needle placement compared to preoperative imaging methods such as the MRI. The study proposed by Kubelick et al. evaluated the performance of the technique with MRI modality as the reference standard (Kubelick and Emelianov, 2020a; Kubelick and Emelianov, 2020b). The team utilized both PA/US and MRI modalities to track tagged stem cells in the spinal cord. The experiment result revealed strong agreement between the PA/US and MRI images. Notably, the PA/US modality demonstrated a minimum detectable cell concentration (100 cells/μL) that is ten times higher compared to MRI and also shows advantages in terms of real-time imaging, portability, and footprint size. Although the team stated the imaging depth to be the limit of the PA/US modality, they believe that incorporating previously published innovation detection mechanisms can enhance the current imaging modality (Kubelick et al., 2019; Demissie et al., 2020). It is worth mentioning that the characteristics of PA/US needle guidance extends beyond stem cell injection. Studies have proved PA/US to be a viable tool for other minimally invasive procedures such as brachytherapy (Su et al., 2011) and nerve blocks revolutionize (Xia et al., 2016). These studies have reported minimized radiation exposure and improved delivery precision with PA/US guidance, indicating its potential to enhance treatment outcomes and reduce side effects.

While promising preclinical studies have demonstrated the feasibility and potential of PA/US for stem cell tracking, the clinical translation of this technique is still limited at the current time. The application of dual-modal exogenous contrast agents can enhance the specificity and sensitivity of the system, enabling precise localization and monitoring of stem cell populations *in vivo*. Therefore, one of the key aspects of the clinical transformation of PA/US is the validation of the safety, efficacy, and reliability of the contrast agents in human subjects. Validating the contrast agents for clinical use involves longitudinal studies to investigate the long-term behavior of transplanted stem cells and assess their therapeutic outcomes. Additionally, it necessitates the establishment of regulatory standards and the acquisition of appropriate certifications. This process is time-consuming and requires scrutiny to ensure patient safety and optimize clinical efficacy. To expedite the clinical translation of PA/US, it may be advantageous to focus efforts on optimizing existing molecules that have already received approval from regulatory bodies such as the FDA (Moore et al., 2019) for prolonged retention within the cells and strong PA signal generation.

Another aspect to consider is that existing contrast agents employed in PA/US provide limited functional information beyond the location of the labeled cells that have been implanted. Therefore, developing standardized and validated quantitative analysis techniques for PA/US imaging of stem cells is crucial for clinical translation. Quantitative imaging goes beyond merely tracking the migration of stem cells; it has the potential to offer immediate feedback on the status of transplanted stem cells, guide procedures during stem cell transplantation, and monitor potential immune responses or adverse reactions. This capability holds tremendous potential for revolutionizing regenerative medicine and deserves more attention in future work.

4 Discussion and outlook

As discussed in the previous section, a dual-modal approach provides more insight into organ or tissue characteristics. In contrast to imaging configurations that require a significant amount of time ranging from minutes to hours, researchers are increasingly adopting tomographic PA/US configurations for clinical use. The combination of metabolic, vascular, and structural information provides a holistic view of the pathology, offering the potential for precise diagnosis and individualized treatment, ultimately leading to better patient outcomes. Continued research and development in the integration of PA/US with other modalities will drive advancements for PA/US oral imaging and its clinical applications.

In this review, we mostly focused on preclinical and clinical applications of integrated PA/US systems with some insight into future clinical translation. Independently, the field of PA imaging has seen tremendous growth over the past 2 decades. Research and development have focused primarily on miniaturizing the light source, improving the imaging depth and speed, and enhancing the image quality. Compact light delivery systems, such as laser diodes, and LEDs are being studied, which could lead to portable and wearable PA devices (Hariri et al., 2018; Zhong et al., 2018; Fatima et al., 2019; Kuniyil Ajith Singh and Xia, 2020; Zhu et al., 2020). Replacing the laser with an LED significantly reduces the system cost. While the optical energy is much lower for an LED, it opens the door for point-of-care applications.

With novel contrast agents and super-resolution imaging (Conkey et al., 2015), deeper imaging has been made possible (Chitgupi et al., 2019; Fu et al., 2019; Li et al., 2020; Han et al., 2022). With obesity becoming a global epidemic, this is especially useful. Ultrasound signal gets attenuated and scattered as tissue thickness increases, especially adipose (Glanc et al., 2012; Uppot, 2018; Heinitz et al., 2023). Real-time imaging is being developed by utilizing fast scanning mechanisms and lasers with higher repetition rates (Manwar et al., 2018; Jeon et al., 2019; Kim et al., 2020a). This is especially needed for IVUS/IVPA systems where it maybe imperative for the operator to adjust imaging parameters with real-time feedback. It is also essential to catheter positioning for precision, as well as to analyze any identified are of concern.

Detection systems with various transducer geometries have evolved (Nyayapathi and Xia, 2019; Manwar et al., 2020). Numerous groups have been devoted to developing more advanced imaging hardware to enhance the performance of the PA/US modality, and novel transducers play a significant role in this endeavor. For the US modality, the US transducers are typically placed close to the imaging target to reduce acoustic attenuation. However, the transducer might also block light delivery. The transparent transducers provide direct light delivery through the transducer (Park et al., 2021b; Ren et al., 2021) (Figures 15A,B).

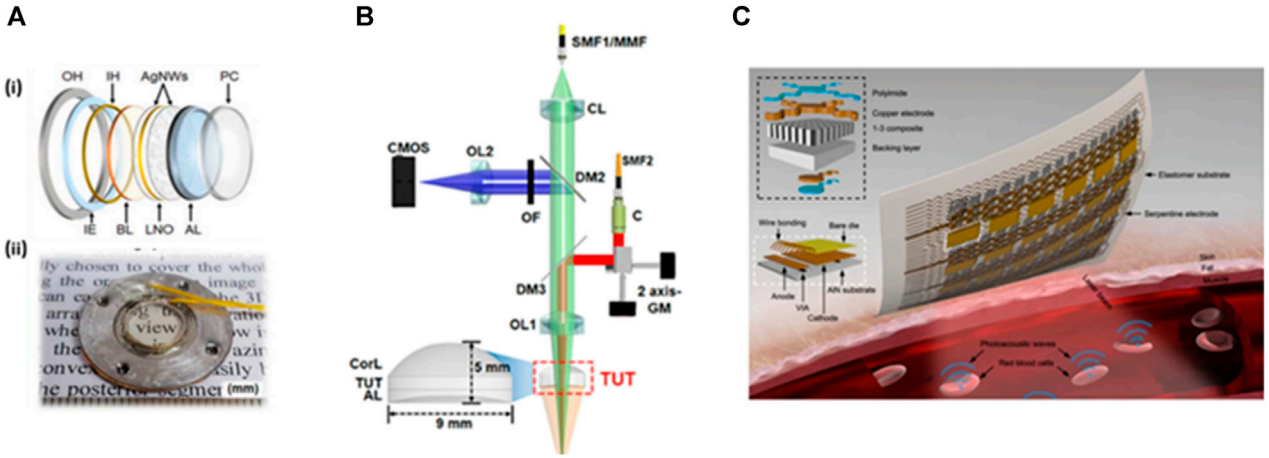

FIGURE 15
Advanced transducer designs (transparent, wearable). **(A)** (i) Schematic (ii) Photograph of a transparent transducer for PA/US dual-modal imaging. PC: parylene coating layer; AL: acoustic lens; LNO: lithium niobite; AgNWs: silver nanowires; BL: backing layer; IH: inner housing; IE: insulation epoxy; OH: outer housing; **(B)** Schematic drawing of integrated imaging system using a transparent US transducer (TUT). CL, collimation lens; OL: objective lens; DM: dichroic beamsplitter; C, collimator; CorL, correction lens; CMOS: complementary metal oxide semiconductor; SMF: single-mode fiber. **(C)** Schematic of the wearable PA/US dual-modal patch. The patch contains VCSELs as the light source and a piezoelectric transducer array for signal detection. Reproduced with permission from (Park et al., 2021b; Gao et al., 2022).

While the low piezoelectricity of the transducer material can affect the system performance, a two-matching-layer design can solve this issue (Chen et al., 2021). The transparent transducer's ability to perform co-axial dual-modal imaging with reduced system complexity and cost (Park et al., 2020a) makes it a viable tool for various clinical applications, such as ophthalmology (Park et al., 2021c), oncology (Park et al., 2022), and intravascular imaging (Yildiz et al., 2018; Li et al., 2019; Wu et al., 2019). The same design is also applied in PAM system to replace traditional reflectors for less acoustic loss (Park et al., 2020b).

In addition to transparent transducers, other novel transducer designs have also been proposed. As shown in Figure 15C, Gao et al., 2022 developed a wearable PA/US soft patch comprised of vertical-cavity surface-emitting lasers (VCSEL) and piezoelectric transducer elements, all integrated into a flexible pad. The patch allows noninvasive continuous mapping of the volumetric distributions of hemoglobin and core temperature at a depth beyond the skin surface. In conjunction with recent advances in wearable ultrasound (Wang et al., 2022), we envision a wearable PA/US sensing patch can be developed for wellness monitoring and imaging. The US modality can be integrated with PA without additional pulse-receive circuits, by generating US pulses from the "clutter" PA signals generated by the absorption of backscattered laser radiation by the metalized surface of the PA detector (Subochev et al., 2015; Johnson et al., 2018). As the same laser is used for both PA and US excitation, the system compactness is greatly improved.

Vast improvements have also been made to reconstruction methods. US interferometry can assess the acoustic inhomogeneity of tissue based on the correlation and phase difference between adjacent receiver locations. Yin et al., 2015 used US interferometry in conjunction with a subsequent time-reversal algorithm to recover PA images from scattered signals. This approach eliminated the influence of acoustic inhomogeneity on PA image quality. For the same purpose, PA and US tomography (PACT/USCT) have been combined to simultaneously estimate the initial pressure distributions and speed of sound (Xia et al., 2013b; Matthews and Anastasio, 2017a). A PA-guided focused US imaging method has also been proposed to reduce reflection artifacts caused by PA sources (Kuniyil Ajith Singh and Steenbergen, 2015). The US focal zone is set to match the optical absorber to start the signal acquisition. The US signal thus mimics PA acquisition to aid the identification of PA reflectors in tissue.

On the other hand, Biswas et al., 2015 used US reflection imaging to address reflection artifacts from the bone caused by PA backscattering at the bone surface. The bone surface is determined using a pulse-echo algorithm that considers one pulse/receiver pair at a time, with the epidermis assumed to be the US transmitter and the PA probe assumed to be the detector array. This reconstruction method was verified to be especially useful for reflectors, as it is effective at detecting joint spaces and reducing reflection artifacts in images containing highly scattering materials.

Recent development various artificial intelligence (AI) has provided multiple tools to improve PA imaging. Recent works have been geared towards improving PA image acquisition, detection, resolution, and overall quality (Zhang et al., 2021; Bell, 2022). Many deep learning-based PA reconstruction methods have been proposed to overcome the limited detection view and low image contrast problems for real-time (Kim et al., 2020b), raw and beamformed images (LanY-Net et al., 2020), linear arrays (Zhang et al., 2021), ring-shaped arrays (Zhang et al., 2020), and many more (Hauptmann et al., 2018; Schwab et al., 2019). Gröhl et al., 2021; Hsu et al., 2021; Yang et al., 2021 have provided comprehensive reviews regarding PA image reconstruction. Furthermore, quantitative photoacoustic imaging (qPAT), in which the quantitative optical absorption coefficient map is

obtained by combining PAT with light transport models, are being studied to improve PA reconstruction. Thus, qPAT can provide highly accurate concentration estimates of chromophores with an optical inversion before spectral unmixing, which corrects for the effect of fluence. Various researchers are now working on this novel method to study disease progression and molecular imaging (Cox et al., 2012; Cook et al., 2013; Bench et al., 2020; Wang et al., 2023b).

US imaging has also seen exponential growth in the past decade. AI tools have been used to improve and/or replace conventional US beamforming (Khan et al., 2020; Luijten et al., 2020). Furthermore, the use of AI has shown great promise in speckle suppression (Hyun et al., 2019), segmentation (Ronneberger et al., 2015), and overall improvement in image quality (Litjens et al., 2017). Quantitative US features like acoustic backscatter and attenuation are being studied to map heterogeneity in tissue (Tai et al., 2020; Basavarajappa et al., 2021). Plane-wave imaging and parallel beamforming-based ultrafast US are being developed with potential in various applications (Tanter and Fink, 2014; Baranger et al., 2021). 2D transducer arrays are being developed to facilitate 3D imaging in real time (Huang and Zeng, 2017). Other than traditional B-mode US and Doppler, elastography and microvascular ultrasound are catching up with mainstream clinical use (Nenadic et al., 2019; Gu et al., 2022).

Additionally, researchers are investigating the integration of other modalities with PA/US systems to enhance disease monitoring and diagnosis. PA/US systems have been integrated with modalities such as diffuse optical tomography (Bauer et al., 2011), optical coherence tomography (Zhang et al., 2011; Park et al., 2021b), magnetic resonance imaging (Park et al., 2017), near infrared fluorescence (Kim et al., 2010), and confocal microscopy (Liu et al., 2019). Various contrast agents are being developed with applications for dual-modal detection (Lu et al., 2018; Xu et al., 2021; Ye et al., 2021). PA/US dual-modal contrast agents like micro or nanobubbles could be used to assess tumor boundaries during surgery. With advancements in both technologies, each of which provides distinct insights into human biology, the future shows a compelling need to use dual-modal systems in the clinic. PA/US imaging overall shows great potential for clinical translation in all the applications discussed in this review. However, given the rapid advances in the field, there is also a compelling need to standardize PA/US features. In addition, appropriate verification, validation, and safety measures need to be employed. The future shows great promise as improved dual-modal systems will enable clinicians to make more accurate diagnoses and custom treatment plans for patients.

Author contributions

NN: Conceptualization, Formal Analysis, Writing–original draft, Writing–review and editing. EZ: Conceptualization, Formal Analysis, Writing–original draft, Writing–review and editing. QZ: Writing–review and editing. MD: Writing–review and editing, Conceptualization, Funding acquisition, Resources. JX: Conceptualization, Writing–review and editing, Funding acquisition, Resources.

Funding

The author(s) declare financial support was received for the research, authorship, and/or publication of this article. This work was supported by grants from the National Institutes of Health (R01EB029596, R01EB028978, and R01EB032337).

Conflict of interest

The authors declare that the research was conducted in the absence of any commercial or financial relationships that could be construed as a potential conflict of interest.

The author(s) declared that they were an editorial board member of Frontiers, at the time of submission. This had no impact on the peer review process and the final decision.

Publisher's note

All claims expressed in this article are solely those of the authors and do not necessarily represent those of their affiliated organizations, or those of the publisher, the editors and the reviewers. Any product that may be evaluated in this article, or claim that may be made by its manufacturer, is not guaranteed or endorsed by the publisher.

References

Abran, M., Cloutier, G., Cardinal, M. H. R., Chayer, B., Tardif, J. C., and Lesage, F. (2014). Development of a photoacoustic, ultrasound and fluorescence imaging catheter for the study of atherosclerotic plaque. *IEEE Trans. Biomed. Circuits Syst.* 8 (5), 696–703. doi:10.1109/tbcas.2014.2360560

Agrawal, S., Johnstonbaugh, K., Clark, J. Y., Raman, J. D., Wang, X., and Kothapalli, S. R. (2020). Design, development, and multi-characterization of an integrated clinical transrectal ultrasound and photoacoustic device for human prostate imaging. *Diagnostics* 10 (8), 566. doi:10.3390/diagnostics10080566

Allen, T. J., and Beard, P. C. (2009). "Photoacoustic characterisation of vascular tissue at NIR wavelengths," in *Photons plus ultrasound: imaging and sensing 2009* (USA: SPIE).

Amidi, E., Mostafa, A., Nandy, S., Yang, G., Middleton, W., Siegel, C., et al. (2019). Classification of human ovarian cancer using functional, spectral, and imaging features obtained from *in vivo* photoacoustic imaging. *Biomed. Opt. Express* 10 (5), 2303–2317. doi:10.1364/boe.10.002303

Ang, T. L., Kwek, A. B. E., and Wang, L. M. (2018). Diagnostic endoscopic ultrasound: technique, current status and future directions. *Gut Liver* 12 (5), 483–496. doi:10.5009/gnl17348

Arthuis, C. J., Novell, A., Raes, F., Escoffre, J. M., Lerondel, S., Le Pape, A., et al. (2017). Real-time monitoring of placental oxygenation during maternal hypoxia and hyperoxygenation using photoacoustic imaging. *PLOS ONE* 12 (1), e0169850. doi:10.1371/journal.pone.0169850

Asao, Y., Hashizume, Y., Suita, T., Nagae, K. i., Fukutani, K., Sudo, Y., et al. (2016). Photoacoustic mammography capable of simultaneously acquiring photoacoustic and ultrasound images. *J. Biomed. Opt.* 21 (11), 116009. doi:10.1117/1.jbo.21.11.116009

Attia, A. B. E., Balasundaram, G., Moothanchery, M., Dinish, U., Bi, R., Ntziachristos, V., et al. (2019). A review of clinical photoacoustic imaging: current and future trends. *Photoacoustics* 16, 100144. doi:10.1016/j.pacs.2019.100144

Baranger, J., Demene, C., Frerot, A., Faure, F., Delanoë, C., Serroune, H., et al. (2021). Bedside functional monitoring of the dynamic brain connectivity in human neonates. *Nat. Commun.* 12 (1), 1080–1110. doi:10.1038/s41467-021-21387-x

Barbour, K. E., Helmick, C. G., Boring, M., and Brady, T. J. (2017). Vital signs: prevalence of doctor-diagnosed arthritis and arthritis-attributable activity limitation - United States, 2013-2015. *MMWR Morb. Mortal. Wkly. Rep.* 66 (9), 246–253. doi:10.15585/mmwr.mm6609e1

Bar-Zion, A., Yin, M., Adam, D., and Foster, F. S. (2016). Functional flow patterns and static blood pooling in tumors revealed by combined contrast-enhanced ultrasound and photoacoustic imaging. *Cancer Res.* 76 (15), 4320–4331. doi:10.1158/0008-5472.can-16-0376

Basavarajappa, L., Baek, J., Reddy, S., Song, J., Tai, H., Rijal, G., et al. (2021). Multiparametric ultrasound imaging for the assessment of normal versus steatotic livers. *Sci. Rep.* 11 (1), 2655. doi:10.1038/s41598-021-82153-z

Bauer, A. Q., Nothdurft, R. E., Erpelding, T. N., Wang, L. V., and Culver, J. P. (2011). Quantitative photoacoustic imaging: correcting for heterogeneous light fluence distributions using diffuse optical tomography. *J. Biomed. Opt.* 16 (9), 096016. doi:10.1117/1.3626212

Bayer, C. L., Wlodarczyk, B. J., Finnell, R. H., and Emelianov, S. Y. (2017). Ultrasound-guided spectral photoacoustic imaging of hemoglobin oxygenation during development. *Biomed. Opt. Express* 8 (2), 757–763. doi:10.1364/boe.8.000757

Beard, P. (2011a). Biomedical photoacoustic imaging. *Interface Focus* 1 (4), 602–631. doi:10.1098/rsfs.2011.0028

Bell, M. A. L. (2022). "Photoacoustic image formation and surgical guidance with machine learning," in *Frontiers in optics* (Washington: Optica Publishing Group).

Bench, C., Hauptmann, A., and Cox, B. (2020). Toward accurate quantitative photoacoustic imaging: learning vascular blood oxygen saturation in three dimensions. *J. Biomed. Opt.* 25 (8), 085003. doi:10.1117/1.jbo.25.8.085003

Biswas, S. K., van Es, P., Steenbergen, W., and Manohar, S. (2015). A method for delineation of bone surfaces in photoacoustic computed tomography of the finger. *Ultrason. Imaging* 38 (1), 63–76. doi:10.1177/0161734615589288

Boyko, E. J., Monteiro-Soares, M., and Wheeler, S. G. (2018). Peripheral arterial disease, foot ulcers, lower extremity amputations, and diabetes. *Diabetes Am.*

Breathnach, A., Concannon, E., Dorairaj, J. J., Shaharan, S., McGrath, J., Jose, J., et al. (2018). Preoperative measurement of cutaneous melanoma and nevi thickness with photoacoustic imaging. *J. Med. Imaging (Bellingham)* 5 (1), 1. doi:10.1117/1.jmi.5.1.015004

Breathnach, A., et al. (2015a). Assessment of cutaneous melanoma and pigmented skin lesions with photoacoustic imaging. *Photonic Ther. Diagnostics Xi*, 9303. doi:10.1117/12.2078309

Breathnach, A., et al. (2015b). "Assessment of cutaneous melanoma and pigmented skin lesions with photoacoustic imaging," in *Photonic therapeutics and diagnostics XI* (USA: SPIE).

Briggs, K., Al Mahrouki, A., Nofiele, J., El-Falou, A., Stanisz, M., Kim, H. C., et al. (2014). Non-invasive monitoring of ultrasound-stimulated microbubble radiation enhancement using photoacoustic imaging. *Technol. cancer Res. Treat.* 13 (5), 435–444. doi:10.7785/tcrtexpress.2013.600266

Cao, Y., Kole, A., Hui, J., Zhang, Y., Mai, J., Alloosh, M., et al. (2018). Fast assessment of lipid content in arteries *in vivo* by intravascular photoacoustic tomography. *Sci. Rep.* 8 (1), 2400. doi:10.1038/s41598-018-20881-5

Chen, H., Mirg, S., Osman, M., Agrawal, S., Cai, J., Biskowitz, R., et al. (2021). A high sensitivity transparent ultrasound transducer based on PMN-PT for ultrasound and photoacoustic imaging. *IEEE Sens. Lett.* 5 (11), 1–4. doi:10.1109/lsens.2021.3122097

Chitgupi, U., Nyayapathi, N., Kim, J., Wang, D., Sun, B., Li, C., et al. (2019). Surfactant-stripped micelles for NIR-II photoacoustic imaging through 12 cm of breast tissue and whole human breasts. *Adv. Mater.* 31 (40), 1902279. doi:10.1002/adma.201902279

Cho, N. H., Shaw, J., Karuranga, S., Huang, Y., da Rocha Fernandes, J., Ohlrogge, A., et al. (2018). IDF Diabetes Atlas: global estimates of diabetes prevalence for 2017 and projections for 2045. *Diabetes Res. Clin. Pract.* 138, 271–281. doi:10.1016/j.diabres.2018.02.023

Choi, W., Park, E. Y., Jeon, S., and Kim, C. (2018). Clinical photoacoustic imaging platforms. *Biomed. Eng. Lett.* 8 (2), 139–155. doi:10.1007/s13534-018-0062-7

Choi, W., Park, E. Y., Jeon, S., Yang, Y., Park, B., Ahn, J., et al. (2022). Three-dimensional multistructural quantitative photoacoustic and US imaging of human feet *in vivo*. *Radiology* 303 (2), 467–473. doi:10.1148/radiol.211029

Christensen-Jeffries, K., Couture, O., Dayton, P. A., Eldar, Y. C., Hynynen, K., Kiessling, F., et al. (2020). Super-resolution ultrasound imaging. *Ultrasound Med. Biol.* 46 (4), 865–891. doi:10.1016/j.ultrasmedbio.2019.11.013

Chung, E., Nam, S. Y., Ricles, L. M., Emelianov, S., and Suggs, L. (2013). Evaluation of gold nanotracers to track adipose-derived stem cells in a PEGylated fibrin gel for dermal tissue engineering applications. *Int. J. Nanomedicine* 8, 325–336. doi:10.2147/ijn.s36711

Clarke-Pearson, D. L. (2009). Screening for ovarian cancer. *N. Engl. J. Med.* 361 (2), 170–177. doi:10.1056/nejmcp0901926

Conkey, D. B., Caravaca-Aguirre, A. M., Dove, J. D., Ju, H., Murray, T. W., and Piestun, R. (2015). Super-resolution photoacoustic imaging through a scattering wall. *Nat. Commun.* 6 (1), 7902–7907. doi:10.1038/ncomms8902

Constans, C., Deffieux, T., Pouget, P., Tanter, M., and Aubry, J. F. (2017). A 200–1380-kHz quadrifrequency focused ultrasound transducer for neurostimulation in rodents and primates: transcranial *in vitro* calibration and numerical study of the influence of skull cavity. *IEEE Trans. ultrasonics, Ferroelectr. Freq. control* 64 (4), 717–724. doi:10.1109/tuffc.2017.2651648

Cook, J. R., Frey, W., and Emelianov, S. (2013). Quantitative photoacoustic imaging of nanoparticles in cells and tissues. *ACS Nano* 7 (2), 1272–1280. doi:10.1021/nn304739s

Couture, O., Hingot, V., Heiles, B., Muleki-Seya, P., and Tanter, M. (2018). Ultrasound localization microscopy and super-resolution: a state of the art. *IEEE Trans. Ultrason. Ferroelectr. Freq. Control* 65 (8), 1304–1320. doi:10.1109/tuffc.2018.2850811

Cox, B., Laufer, J. G., Arridge, S. R., and Beard, P. C. (2012). Quantitative spectroscopic photoacoustic imaging: a review. *J. Biomed. Opt.* 17 (6), 061202. doi:10.1117/1.jbo.17.6.061202

Daoudi, K., Kersten, B. E., van den Ende, C. H. M., van den Hoogen, F. H. J., Vonk, M. C., and de Korte, C. L. (2021). Photoacoustic and high-frequency ultrasound imaging of systemic sclerosis patients. *Arthritis Res. Ther.* 23 (1), 22. doi:10.1186/s13075-020-02400-y

Daoudi, K., van den Berg, P., Rabot, O., Kohl, A., Tisserand, S., Brands, P., et al. (2014). Handheld probe integrating laser diode and ultrasound transducer array for ultrasound/photoacoustic dual modality imaging. *Opt. Express* 22 (21), 26365–26374. doi:10.1364/oe.22.026365

Das, D., Sharma, A., Rajendran, P., and Pramanik, M. (2021). Another decade of photoacoustic imaging. *Phys. Med. Biol.* 66 (5), 05TR01. doi:10.1088/1361-6560/abd669

Dean-Ben, X. L., and Razansky, D. (2021). Optoacoustic imaging of the skin. *Exp. Dermatol* 30 (11), 1598–1609. doi:10.1111/exd.14386

Demene, C., Baranger, J., Bernal, M., Delanoe, C., Auvin, S., Biran, V., et al. (2017). Functional ultrasound imaging of brain activity in human newborns. *Sci. Transl. Med.* 9 (411), eaah6756. doi:10.1126/scitranslmed.aah6756

Demissie, A. A., VanderLaan, D., Islam, M. S., Emelianov, S., and Dickson, R. M. (2020). Synchronously amplified photoacoustic image recovery (SAPhIRe). *Photoacoustics* 20, 100198. doi:10.1016/j.pacs.2020.100198

DeVore, G. R., Satou, G., and Sklansky, M. (2017). 4D fetal echocardiography—an update. *Echocardiography* 34 (12), 1788–1798. doi:10.1111/echo.13708

Dhillon, J., Thorwald, M., Chung, S., Maloney, G., and Srivatsa, S. (2020). Comparison of hand-held acoustic Doppler with point-of-care portable color Doppler ultrasound in the assessment of venous reflux disease. *J. Vasc. Surg. Venous Lymphatic Disord.* 8 (5), 831–839. e2. doi:10.1016/j.jvsv.2019.11.020

Donnelly, E. M., Kubelick, K. P., Dumani, D. S., and Emelianov, S. Y. (2018). Photoacoustic image-guided delivery of plasmonic-nanoparticle-labeled mesenchymal stem cells to the spinal cord. *Nano Lett.* 18 (10), 6625–6632. doi:10.1021/acs.nanolett.8b03305

Duric, N., Littrup, P., Babkin, A., Chambers, D., Azevedo, S., Kalinin, A., et al. (2005). Development of ultrasound tomography for breast imaging: technical assessment. *Med. Phys.* 32 (5), 1375–1386. doi:10.1118/1.1897463

Eisenstein, M. (2023). A sound solution for deep-brain imaging. *Nat. Methods* 20 (11), 1623–1628. doi:10.1038/s41592-023-02055-y

Estrada, H., Ozbek, A., Robin, J., Shoham, S., and Razansky, D. (2020b). Spherical array system for high-precision transcranial ultrasound stimulation and optoacoustic imaging in rodents. *IEEE Trans. ultrasonics, Ferroelectr. Freq. control* 68 (1), 107–115. doi:10.1109/tuffc.2020.2994877

Estrada, H., Rebling, J., Sievert, W., Hladik, D., Hofmann, U., Gottschalk, S., et al. (2020a). Intravital optoacoustic and ultrasound bio-microscopy reveal radiation-inhibited skull angiogenesis. *Bone* 133, 115251. doi:10.1016/j.bone.2020.115251

Falk, E., Shah, P. K., and Fuster, V. (1995). Coronary plaque disruption. *Circulation* 92 (3), 657–671. doi:10.1161/01.cir.92.3.657

Fatakdawala, H., Poti, S., Zhou, F., Sun, Y., Bec, J., Liu, J., et al. (2013a). Multimodal *in vivo* imaging of oral cancer using fluorescence lifetime, photoacoustic and ultrasound techniques. *Biomed. Opt. Express* 4 (9), 1724–1741. doi:10.1364/boe.4.001724

Fatima, A., Kratkiewicz, K., Manwar, R., Zafar, M., Zhang, R., Huang, B., et al. (2019). Review of cost reduction methods in photoacoustic computed tomography. *Photoacoustics* 15, 100137. doi:10.1016/j.pacs.2019.100137

Feldchtein, F. I., Gelikonov, G. V., Gelikonov, V. M., Iksanov, R. R., Kuranov, R. V., Sergeev, A. M., et al. (1998). *In vivo* OCT imaging of hard and soft tissue of the oral cavity. *Opt. Express* 3 (6), 239–250. doi:10.1364/oe.3.000239

Ferlay, J., Soerjomataram, I., Dikshit, R., Eser, S., Mathers, C., Rebelo, M., et al. (2015). Cancer incidence and mortality worldwide: sources, methods and major patterns in GLOBOCAN 2012. *Int. J. cancer* 136 (5), E359–E386. doi:10.1002/ijc.29210

Francis, K. J., Boink, Y. E., Dantuma, M., Ajith Singh, M. K., Manohar, S., and Steenbergen, W. (2020). Tomographic imaging with an ultrasound and LED-based photoacoustic system. *Biomed. Opt. express* 11 (4), 2152–2165. doi:10.1364/boe.384548

Fu, L., et al. (2022). Full-mouth photoacoustic/ultrasound imaging of the periodontal pocket with a compact intraoral transducer. *bioRxiv*. doi:10.1101/2022.03.31.486608

Fu, Q., Zhu, R., Song, J., Yang, H., and Chen, X. (2019). Photoacoustic imaging: contrast agents and their biomedical applications. *Adv. Mater.* 31 (6), 1805875. doi:10.1002/adma.201805875

Fujii, T., Nagamatsu, T., Morita, K., Schust, D. J., Iriyama, T., Komatsu, A., et al. (2017). Enhanced HIF2α expression during human trophoblast differentiation into syncytiotrophoblast suppresses transcription of placental growth factor. *Sci. Rep.* 7 (1), 12455. doi:10.1038/s41598-017-12685-w

Galanzha, E. I., Menyaev, Y. A., Yadem, A. C., Sarimollaoglu, M., Juratli, M. A., Nedosekin, D. A., et al. (2019). *In vivo* liquid biopsy using Cytophone platform for photoacoustic detection of circulating tumor cells in patients with melanoma. *Sci. Transl. Med.* 11 (510), eaat5857. doi:10.1126/scitranslmed.aat5857

Gao, X., Chen, X., Hu, H., Wang, X., Yue, W., Mu, J., et al. (2022). A photoacoustic patch for three-dimensional imaging of hemoglobin and core temperature. *Nat. Commun.* 13 (1), 7757. doi:10.1038/s41467-022-35455-3

Garcia-Barros, M., Paris, F., Cordon-Cardo, C., Lyden, D., Rafii, S., Haimovitz-Friedman, A., et al. (2003). Tumor response to radiotherapy regulated by endothelial cell apoptosis. *Science* 300 (5622), 1155–1159. doi:10.1126/science.1082504

Gardner, C. M., Tan, H., Hull, E. L., Lisauskas, J. B., Sum, S. T., Meese, T. M., et al. (2008). Detection of lipid core coronary plaques in autopsy specimens with a novel catheter-based near-infrared spectroscopy system. *JACC Cardiovasc. Imaging* 1 (5), 638–648. doi:10.1016/j.jcmg.2008.06.001

Gennisson, J.-L., Deffieux, T., Fink, M., and Tanter, M. (2013). Ultrasound elastography: principles and techniques. *Diagnostic interventional imaging* 94 (5), 487–495. doi:10.1016/j.diii.2013.01.022

Gharib, H., Papini, E., Garber, J. R., Duick, D. S., Harrell, R. M., Hegedüs, L., et al. (2016). AMERICAN ASSOCIATION OF CLINICAL ENDOCRINOLOGISTS, AMERICAN COLLEGE OF ENDOCRINOLOGY, AND ASSOCIAZIONE MEDICI ENDOCRINOLOGI MEDICAL GUIDELINES FOR CLINICAL PRACTICE FOR THE DIAGNOSIS AND MANAGEMENT OF THYROID NODULES--2016 UPDATE. *Endocr. Pract.* 22 (5), 622–639. doi:10.4158/EP161208.GL

Gilbert, J., Dukes, M., Lamarca, B., Cockrell, K., Babcock, S., and Granger, J. (2007). Effects of reduced uterine perfusion pressure on blood pressure and metabolic factors in pregnant rats*. *Am. J. Hypertens.* 20 (6), 686–691. doi:10.1016/j.amjhyper.2006.12.016

Gilbert, J. S., Gilbert, S. A., Arany, M., and Granger, J. P. (2009). Hypertension produced by placental ischemia in pregnant rats is associated with increased soluble endoglin expression. *Hypertension* 53 (2), 399–403. doi:10.1161/hypertensionaha.108.123513

Glanc, P., O'Hayon, B. E., Singh, D. K., Bokhari, S. A. J., and Maxwell, C. V. (2012). Challenges of pelvic imaging in obese women. *RadioGraphics* 32 (6), 1839–1862. doi:10.1148/rg.326125510

Goldie, I. (1969). The synovial microvascular derangement in rheumatoid arthritis and osteoarthritis. *Acta Orthop. Scand.* 40 (6), 751–764. doi:10.3109/17453676908989539

Gröhl, J., Schellenberg, M., Dreher, K., and Maier-Hein, L. (2021). Deep learning for biomedical photoacoustic imaging: a review. *Photoacoustics* 22, 100241. doi:10.1016/j.pacs.2021.100241

Gu, J., Ternifi, R., Larson, N. B., Carter, J. M., Boughey, J. C., Stan, D. L., et al. (2022). Hybrid high-definition microvessel imaging/shear wave elastography improves breast lesion characterization. *Breast Cancer Res.* 24 (1), 16–13. doi:10.1186/s13058-022-01511-5

Guo, B., Sheng, Z., Kenry, K., Hu, D., Lin, X., Xu, S., et al. (2017). Biocompatible conjugated polymer nanoparticles for highly efficient photoacoustic imaging of orthotopic brain tumors in the second near-infrared window. *Mater. Horizons* 4 (6), 1151–1156. doi:10.1039/c7mh00672a

Guo, H., Qi, W., He, M., Rong, J., and Xi, L. (2018). Co-registered photoacoustic and ultrasound imaging for tongue cancer detection. *J. Innovative Opt. Health Sci.* 11 (3). doi:10.1142/s1793545818500086

Guo, H., Wang, Q., Qi, W., Sun, X., Ke, B., and Xi, L. (2019). Assessing the development and treatment of rheumatoid arthritis using multiparametric photoacoustic and ultrasound imaging. *J. Biophot.* 12 (11), e201900127. doi:10.1002/jbio.201900127

Han, S., Lee, D., Kim, S., Kim, H. H., Jeong, S., and Kim, J. (2022). Contrast agents for photoacoustic imaging: a review focusing on the wavelength range. *Biosensors* 12 (8), 594. doi:10.3390/bios12080594

Hariri, A., Lemaster, J., Wang, J., Jeevarathinam, A. S., Chao, D. L., and Jokerst, J. V. (2018). The characterization of an economic and portable LED-based photoacoustic imaging system to facilitate molecular imaging. *Photoacoustics* 9, 10–20. doi:10.1016/j.pacs.2017.11.001

Hartman, R. K., Hallam, K. A., Donnelly, E. M., and Emelianov, S. Y. (2019). Photoacoustic imaging of gold nanorods in the brain delivered via microbubble-assisted focused ultrasound: a tool for *in vivo* molecular neuroimaging. *Laser Phys. Lett.* 16 (2), 025603. doi:10.1088/1612-202x/aaf89e

Hauptmann, A., Lucka, F., Betcke, M., Huynh, N., Adler, J., Cox, B., et al. (2018). Model-based learning for accelerated, limited-view 3-D photoacoustic tomography. *IEEE Trans. Med. imaging* 37 (6), 1382–1393. doi:10.1109/tmi.2018.2820382

Heinitz, S., Müller, J., Jenderka, K. V., Schlögl, H., Stumvoll, M., Blüher, M., et al. (2023). The application of high-performance ultrasound probes increases anatomic depiction in obese patients. *Sci. Rep.* 13 (1), 16297. doi:10.1038/s41598-023-43509-9

Hockel, M., and Vaupel, P. (2001). Tumor hypoxia: definitions and current clinical, biologic, and molecular aspects. *J. Natl. Cancer Inst.* 93 (4), 266–276. doi:10.1093/jnci/93.4.266

Hsu, K.-T., Guan, S., and Chitnis, P. V. (2021). Comparing deep learning frameworks for photoacoustic tomography image reconstruction. *Photoacoustics* 23, 100271. doi:10.1016/j.pacs.2021.100271

Hu, S., and Wang, L. V. (2010). Photoacoustic imaging and characterization of the microvasculature. *J. Biomed. Opt.* 15 (1), 011101. doi:10.1117/1.3281673

Huang, C., Cheng, Y., Zheng, W., Bing, R. W., Zhang, H., Komornicki, I., et al. (2023). Dual-scan photoacoustic tomography for the imaging of vascular structure on foot. *IEEE Trans. Ultrasonics, Ferroelectr. Freq. Control* 70 (12), 1703–1713. doi:10.1109/tuffc.2023.3283139

Huang, Q., and Zeng, Z. (2017). A review on real-time 3D ultrasound imaging technology. *BioMed Res. Int.* 2017, 1–20. doi:10.1155/2017/6027029

Hucker, W. J., Ripplinger, C. M., Fleming, C. P., Fedorov, V. V., Rollins, A. M., and Efimov, I. R. (2008). Bimodal biophotonic imaging of the structure-function relationship in cardiac tissue. *J. Biomed. Opt.* 13 (5), 054012. doi:10.1117/1.2975826

Hui, J., Cao, Y., Zhang, Y., Kole, A., Wang, P., Yu, G., et al. (2017). Real-time intravascular photoacoustic-ultrasound imaging of lipid-laden plaque in human coronary artery at 16 frames per second. *Sci. Rep.* 7 (1), 1417. doi:10.1038/s41598-017-01649-9

Hui, J., Li, R., Phillips, E. H., Goergen, C. J., Sturek, M., and Cheng, J. X. (2016). Bond-selective photoacoustic imaging by converting molecular vibration into acoustic waves. *Photoacoustics* 4 (1), 11–21. doi:10.1016/j.pacs.2016.01.002

Hwang, S. Y., Choi, E. S., Kim, Y. S., Gim, B. E., Ha, M., and Kim, H. Y. (2018). Health effects from exposure to dental diagnostic X-ray. *Environ. Health Toxicol.* 33 (4), e2018017. doi:10.5620/eht.e2018017

Hyun, D., Brickson, L. L., Looby, K. T., and Dahl, J. J. (2019). Beamforming and speckle reduction using neural networks. *IEEE Trans. ultrasonics, Ferroelectr. Freq. control* 66 (5), 898–910. doi:10.1109/tuffc.2019.2903795

Imbault, M., Chauvet, D., Gennisson, J. L., Capelle, L., and Tanter, M. (2017). Intraoperative functional ultrasound imaging of human brain activity. *Sci. Rep.* 7 (1), 7304. doi:10.1038/s41598-017-06474-8

Jacques, S. L. (2013). Corrigendum: optical properties of biological tissues: a review. *Phys. Med. Biol.* 58 (14), 5007–5008. doi:10.1088/0031-9155/58/14/5007

Jansen, K., van der Steen, A. F. W., van Beusekom, H. M. M., Oosterhuis, J. W., and van Soest, G. (2011). Intravascular photoacoustic imaging of human coronary atherosclerosis. *Opt. Lett.* 36 (5), 597–599. doi:10.1364/ol.36.000597

Jansen, K., van Soest, G., and van der Steen, A. F. (2014a). Intravascular photoacoustic imaging: a new tool for vulnerable plaque identification. *Ultrasound Med. Biol.* 40 (6), 1037–1048. doi:10.1016/j.ultrasmedbio.2014.01.008

Jansen, K., Wu, M., van der Steen, A. F., and van Soest, G. (2014b). Photoacoustic imaging of human coronary atherosclerosis in two spectral bands. *Photoacoustics* 2 (1), 12–20. doi:10.1016/j.pacs.2013.11.003

Jemal, A., Bray, F., Center, M. M., Ferlay, J., Ward, E., and Forman, D. (2011). Global cancer statistics. *CA a cancer J. Clin.* 61 (2), 69–90. doi:10.3322/caac.20107

Jeon, S., Park, E. Y., Choi, W., Managuli, R., Lee, K. j., and Kim, C. (2019). Real-time delay-multiply-and-sum beamforming with coherence factor for *in vivo* clinical photoacoustic imaging of humans. *Photoacoustics* 15, 100136. doi:10.1016/j.pacs.2019.100136

Jo, J., Xu, G., Cao, M., Marquardt, A., Francis, S., Gandikota, G., et al. (2017). A functional study of human inflammatory arthritis using photoacoustic imaging. *Sci. Rep.* 7 (1), 15026. doi:10.1038/s41598-017-15147-5

Jo, J., Xu, G., Zhu, Y., Burton, M., Sarazin, J., Schiopu, E., et al. (2021). Detecting joint inflammation by an LED-based photoacoustic imaging system: a feasibility study (Erratum). *J. Biomed. Opt.* 26 (5), 059802. doi:10.1117/1.jbo.26.5.059802

Johnson, J. L., Merrilees, M., Shragge, J., and van Wijk, K. (2018). All-optical extravascular laser-ultrasound and photoacoustic imaging of calcified atherosclerotic plaque in excised carotid artery. *Photoacoustics* 9, 62–72. doi:10.1016/j.pacs.2018.01.002

Kalchenko, V., Madar-Balakirski, N., Meglinski, I., and Harmelin, A. (2011). *In vivo* characterization of tumor and tumor vascular network using multi-modal imaging approach. *J. Biophot.* 4 (9), 645–649. doi:10.1002/jbio.201100033

Karpiouk, A. B., Wang, B., and Emelianov, S. Y. (2010). Development of a catheter for combined intravascular ultrasound and photoacoustic imaging. *Rev. Sci. Instrum.* 81 (1), 014901. doi:10.1063/1.3274197

Kerbel, R. S. (2008). Tumor angiogenesis. *N. Engl. J. Med.* 358 (19), 2039–2049. doi:10.1056/nejmra0706596

Khan, S., and Cabanilla, L. L. (2009). Periodontal probing depth measurement: a review. *Compend Contin. Educ. Dent.* 30 (1), 12–36.

Khan, S., Huh, J., and Ye, J. C. (2020). Adaptive and compressive beamforming using deep learning for medical ultrasound. *IEEE Trans. ultrasonics, Ferroelectr. Freq. control* 67 (8), 1558–1572. doi:10.1109/tuffc.2020.2977202

Kim, C., Song, K. H., Gao, F., and Wang, L. V. (2010). Sentinel lymph nodes and lymphatic vessels: noninvasive dual-modality *in vivo* mapping by using indocyanine green in rats—volumetric spectroscopic photoacoustic imaging and planar fluorescence imaging. *Radiology* 255 (2), 442–450. doi:10.1148/radiol.10090281

Kim, J., Park, B., Ha, J., Steinberg, I., Hooper, S. M., Jeong, C., et al. (2021). Multiparametric photoacoustic analysis of human thyroid cancers *in vivo*. *Cancer Res.* 81 (18), 4849–4860. doi:10.1158/0008-5472.can-20-3334

Kim, J., Park, E. Y., Park, B., Choi, W., Lee, K. J., and Kim, C. (2020a). Towards clinical photoacoustic and ultrasound imaging: probe improvement and real-time graphical user interface. *Exp. Biol. Med.* 245 (4), 321–329. doi:10.1177/1535370219889968

Kim, M., Jeng, G. S., Pelivanov, I., and O'Donnell, M. (2020b). Deep-learning image reconstruction for real-time photoacoustic system. *IEEE Trans. Med. imaging* 39 (11), 3379–3390. doi:10.1109/tmi.2020.2993835

Kole, A., Cao, Y., Hui, J., Bolad, I. A., Alloosh, M., Cheng, J. X., et al. (2019). Comparative quantification of arterial lipid by intravascular photoacoustic-ultrasound imaging and near-infrared spectroscopy-intravascular ultrasound. *J. Cardiovasc. Transl. Res.* 12 (3), 211–220. doi:10.1007/s12265-018-9849-2

Kolodgie, F. D., Burke, A. P., Farb, A., Gold, H. K., Yuan, J., Narula, J., et al. (2001). The thin-cap fibroatheroma: a type of vulnerable plaque: the major precursor lesion to acute coronary syndromes. *Curr. Opin. Cardiol.* 16 (5), 285–292. doi:10.1097/00001573-200109000-00006

Kothapalli, S.-R., Sonn, G. A., Choe, J. W., Nikoozadeh, A., Bhuyan, A., Park, K. K., et al. (2019). Simultaneous transrectal ultrasound and photoacoustic human prostate imaging. *Sci. Transl. Med.* 11 (507), eaav2169. doi:10.1126/scitranslmed.aav2169

Kratkiewicz, K., Pattyn, A., Alijabbari, N., and Mehrmohammadi, M. (2022). Ultrasound and photoacoustic imaging of breast cancer: clinical systems, challenges, and future outlook. *J. Clin. Med.* 11 (5), 1165. doi:10.3390/jcm11051165

Kubelick, K. P., and Emelianov, S. Y. (2020a). A trimodal ultrasound, photoacoustic and magnetic resonance imaging approach for longitudinal post-operative monitoring of stem cells in the spinal cord. *Ultrasound Med. Biol.* 46 (12), 3468–3474. doi:10.1016/j.ultrasmedbio.2020.08.026

Kubelick, K. P., and Emelianov, S. Y. (2020b). Prussian blue nanocubes as a multimodal contrast agent for image -guided stem cell therapy of the spinal cord. *Photoacoustics* 18, 100166. doi:10.1016/j.pacs.2020.100166

Kubelick, K. P., Snider, E. J., Ethier, C. R., and Emelianov, S. (2019). Development of a stem cell tracking platform for ophthalmic applications using ultrasound and photoacoustic imaging. *Theranostics* 9 (13), 3812–3824. doi:10.7150/thno.32546

Kuniyil Ajith Singh, M., and Steenbergen, W. (2015). Photoacoustic-guided focused ultrasound (PAFUSion) for identifying reflection artifacts in photoacoustic imaging. *Photoacoustics* 3 (4), 123–131. doi:10.1016/j.pacs.2015.09.001

Kuniyil Ajith Singh, M., and Xia, W. (2020). Portable and affordable light source-based photoacoustic tomography. *Sensors* 20 (21), 6173. doi:10.3390/s20216173

LanY-Net, H., Yang, C., Gao, F., and Gao, F. (2020). Y-Net: hybrid deep learning image reconstruction for photoacoustic tomography *in vivo*. *Photoacoustics* 20, 100197. doi:10.1016/j.pacs.2020.100197

Lawrence, D. J., Escott, M. E., Myers, L., Intapad, S., Lindsey, S. H., and Bayer, C. L. (2019). Spectral photoacoustic imaging to estimate *in vivo* placental oxygenation during preeclampsia. *Sci. Rep.* 9 (1), 558. doi:10.1038/s41598-018-37310-2

Lee, D., Park, S., and Kim, C. (2018). Dual-modal photoacoustic and ultrasound imaging of dental implants. *Photons Plus Ultrasound Imaging Sens.* 2018, 10494. doi:10.1117/12.2286864

Lee, D., Park, S., Noh, W. C., Im, J. S., and Kim, C. (2017). Photoacoustic imaging of dental implants in a porcine jawbone *ex vivo*. *Opt. Lett.* 42 (9), 1760–1763. doi:10.1364/ol.42.001760

Lee, H., Choi, W., Kim, C., Park, B., and Kim, J. (2023). Review on ultrasound-guided photoacoustic imaging for complementary analyses of biological systems *in vivo*. *Exp. Biol. Med. (Maywood)* 248 (9), 762–774. doi:10.1177/15353702231181341

Lee, H.-Y., Després, J.-P., and Koh, K. K. (2013). Perivascular adipose tissue in the pathogenesis of cardiovascular disease. *Atherosclerosis* 230 (2), 177–184. doi:10.1016/j.atherosclerosis.2013.07.037

Leng, H., Wang, Y., Jhang, D. F., Chu, T. S., Tsao, C. H., Tsai, C. H., et al. (2019). Characterization of a fiber bundle-based real-time ultrasound/photoacoustic imaging system and its *in vivo* functional imaging applications. *Micromachines (Basel)* 10 (12), 820. doi:10.3390/mi10120820

Leng, J., Zhang, J., Li, C., Shu, C., Wang, B., et al. (2021). Multi-spectral intravascular photoacoustic/ultrasound/optical coherence tomography tri-modality system with a fully-integrated 0.9-mm full field-of-view catheter for plaque vulnerability imaging. *Biomed. Opt. Express* 12 (4), 1934–1946. doi:10.1364/boe.420724

Leng, X., Chapman, W., Rao, B., Nandy, S., Chen, R., Rais, R., et al. (2018). Feasibility of co-registered ultrasound and acoustic-resolution photoacoustic imaging of human colorectal cancer. *Biomed. Opt. Express* 9 (11), 5159–5172. doi:10.1364/boe.9.005159

Lengenfelder, B., Mehari, F., Hohmann, M., Heinlein, M., Chelales, E., Waldner, M. J., et al. (2019). Remote photoacoustic sensing using speckle-analysis. *Sci. Rep.* 9, 1057. doi:10.1038/s41598-018-38446-x

Li, C., Duric, N., Littrup, P., and Huang, L. (2009). *In vivo* breast sound-speed imaging with ultrasound tomography. *Ultrasound Med. Biol.* 35 (10), 1615–1628. doi:10.1016/j.ultrasmedbio.2009.05.011

Li, D., Humayun, L., Vienneau, E., Vu, T., and Yao, J. (2021). Seeing through the skin: photoacoustic tomography of skin vasculature and beyond. *JID Innov.* 1 (3), 100039. doi:10.1016/j.xjidi.2021.100039

Li, M., Nyayapathi, N., Kilian, H. I., Xia, J., Lovell, J. F., and Yao, J. (2020). Sound out the deep colors: photoacoustic molecular imaging at new depths. *Mol. Imaging* 19, 153601212098151. doi:10.1177/1536012120981518

Li, S. C., Tachiki, L. M. L., Luo, J., Dethlefs, B. A., Chen, Z., and Loudon, W. G. (2010). A biological global positioning system: considerations for tracking stem cell behaviors in the whole body. *Stem Cell. Rev. Rep.* 6 (2), 317–333. doi:10.1007/s12015-010-9130-9

Li, T., and Dewhurst, R. J. (2016). "Near-infrared photoacoustic imaging for detection of early-stage dental diseases," in *Asia-pacific optical sensors conference* (Washington: Optica Publishing Group).

Li, W., Liu, Y. H., Estrada, H., Rebling, J., Reiss, M., Galli, S., et al. (2022). Tracking strain-specific morphogenesis and angiogenesis of murine calvaria with large-scale optoacoustic and ultrasound microscopy. *J. Bone Min. Res.* 37 (5), 1032–1043. doi:10.1002/jbmr.4533

Li, X., Wang, D., Ran, H., Hao, L., Cao, Y., Ao, M., et al. (2018). A preliminary study of photoacoustic/ultrasound dual-mode imaging in melanoma using MAGE-targeted gold nanoparticles. *Biochem. biophysical Res. Commun.* 502 (2), 255–261. doi:10.1016/j.bbrc.2018.05.155

Li, Z., Ilkhechi, A. K., and Zemp, R. (2019). Transparent capacitive micromachined ultrasonic transducers (CMUTs) for photoacoustic applications. *Opt. Express* 27 (9), 13204–13218. doi:10.1364/oe.27.013204

Litjens, G., Kooi, T., Bejnordi, B. E., Setio, A. A. A., Ciompi, F., Ghafoorian, M., et al. (2017). A survey on deep learning in medical image analysis. *Med. image Anal.* 42, 60–88. doi:10.1016/j.media.2017.07.005

Liu, C., Liao, J., Chen, L., Chen, J., Ding, R., Gong, X., et al. (2019). The integrated high-resolution reflection-mode photoacoustic and fluorescence confocal microscopy. *Photoacoustics* 14, 12–18. doi:10.1016/j.pacs.2019.02.001

Liu, Y. B., Wang, Y. T., and Yuan, Z. (2016). Dual-modality imaging of the human finger joint systems by using combined multispectral photoacoustic computed tomography and ultrasound computed tomography. *Biomed Res. Int.* 2016, 1–7. doi:10.1155/2016/1453272

Lu, N., Fan, W., Yi, X., Wang, S., Wang, Z., Tian, R., et al. (2018). Biodegradable hollow mesoporous organosilica nanotheranostics for mild hyperthermia-induced bubble-enhanced oxygen-sensitized radiotherapy. *ACS Nano* 12 (2), 1580–1591. doi:10.1021/acsnano.7b08103

Luijten, B., Cohen, R., de Bruijn, F. J., Schmeitz, H. A. W., Mischi, M., Eldar, Y. C., et al. (2020). Adaptive ultrasound beamforming using deep learning. *IEEE Trans. Med. Imaging* 39 (12), 3967–3978. doi:10.1109/tmi.2020.3008537

Luke, G. P., Yeager, D., and Emelianov, S. Y. (2012a). Biomedical applications of photoacoustic imaging with exogenous contrast agents. *Ann. Biomed. Eng.* 40 (2), 422–437. doi:10.1007/s10439-011-0449-4

Luke, G. P., Yeager, D., and Emelianov, S. Y. (2012b). Biomedical applications of photoacoustic imaging with exogenous contrast agents. *Ann. Biomed. Eng.* 40 (2), 422–437. doi:10.1007/s10439-011-0449-4

Ma, K. F., Kleiss, S. F., Schuurmann, R. C., Bokkers, R. P., Ünlü, Ç., and De Vries, J. P. P. (2019). A systematic review of diagnostic techniques to determine tissue perfusion in patients with peripheral arterial disease. *Expert Rev. Med. devices* 16 (8), 697–710. doi:10.1080/17434440.2019.1644166

Madder, R. D., Puri, R., Muller, J. E., Harnek, J., Götberg, M., VanOosterhout, S., et al. (2016). Confirmation of the intracoronary near-infrared spectroscopy threshold of lipid-rich plaques that underlie ST-segment–elevation myocardial infarction. *Arteriosclerosis, Thrombosis, Vasc. Biol.* 36, 1010–1015. doi:10.1161/atvbaha.115.306849

Mallidi, S., Watanabe, K., Timerman, D., Schoenfeld, D., and Hasan, T. (2015). Prediction of tumor recurrence and therapy monitoring using ultrasound-guided photoacoustic imaging. *Theranostics* 5 (3), 289–301. doi:10.7150/thno.10155

Manohar, S., and Dantuma, M. (2019). Current and future trends in photoacoustic breast imaging. *Photoacoustics* 16, 100134. doi:10.1016/j.pacs.2019.04.004

Manwar, R., Hosseinzadeh, M., Hariri, A., Kratkiewicz, K., Noei, S., and N. Avanaki, M. (2018). Photoacoustic signal enhancement: towards utilization of low energy laser diodes in real-time photoacoustic imaging. *Sensors* 18 (10), 3498. doi:10.3390/s18103498

Manwar, R., Kratkiewicz, K., and Avanaki, K. (2020). Overview of ultrasound detection technologies for photoacoustic imaging. *Micromachines* 11 (7), 692. doi:10.3390/mi11070692

Masuzaki, R., Tateishi, R., Yoshida, H., Sato, T., Ohki, T., Goto, T., et al. (2007). Assessing liver tumor stiffness by transient elastography. *Hepatol. Int.* 1 (3), 394–397. doi:10.1007/s12072-007-9012-7

Matthews, T. P., and Anastasio, M. A. (2017a). Joint reconstruction of the initial pressure and speed of sound distributions from combined photoacoustic and ultrasound tomography measurements. *Inverse Probl.* 33 (12), 124002. doi:10.1088/1361-6420/aa9384

McKenney-Drake, M. L., Rodenbeck, S. D., Bruning, R. S., Kole, A., Yancey, K. W., Alloosh, M., et al. (2017). Epicardial adipose tissue removal potentiates outward remodeling and arrests coronary atherogenesis. *Ann. Thorac. Surg.* 103 (5), 1622–1630. doi:10.1016/j.athoracsur.2016.11.034

Menezes, G. L., Pijnappel, R. M., Meeuwis, C., Bisschops, R., Veltman, J., Lavin, P. T., et al. (2018). Downgrading of breast masses suspicious for cancer by using optoacoustic breast imaging. *Radiology* 288 (2), 355–365. doi:10.1148/radiol.2018170500

Merčep, E., Herraiz, J. L., Deán-Ben, X. L., and Razansky, D. (2019). Transmission–reflection optoacoustic ultrasound (TROPUS) computed tomography of small animals. *Light Sci. Appl.* 8 (1), 18. doi:10.1038/s41377-019-0130-5

Mercep, E., Jeng, G., Morscher, S., Li, P. C., and Razansky, D. (2015). Hybrid optoacoustic tomography and pulse-echo ultrasonography using concave arrays. *Ieee Trans. Ultrasonics Ferroelectr. Freq. Control* 62 (9), 1651–1661. doi:10.1109/tuffc.2015.007058

Mohd-Zahid, M. H., Mohamud, R., Che Abdullah, C. A., Lim, J., Alem, H., Wan Hanaffi, W. N., et al. (2020). Colorectal cancer stem cells: a review of targeted drug delivery by gold nanoparticles. *Rsc Adv.* 10 (2), 973–985. doi:10.1039/c9ra08192e

Moore, C., Bai, Y., Hariri, A., Sanchez, J. B., Lin, C. Y., Koka, S., et al. (2018). Photoacoustic imaging for monitoring periodontal health: a first human study. *Photoacoustics* 12, 67–74. doi:10.1016/j.pacs.2018.10.005

Moore, C., Chen, F., Wang, J., and Jokerst, J. V. (2019). Listening for the therapeutic window: advances in drug delivery utilizing photoacoustic imaging. *Adv. Drug Deliv. Rev.* 144, 78–89. doi:10.1016/j.addr.2019.07.003

Mozaffarzadeh, M., Moore, C., Golmoghani, E. B., Mantri, Y., Hariri, A., Jorns, A., et al. (2021). Motion-compensated noninvasive periodontal health monitoring using handheld and motor-based photoacoustic-ultrasound imaging systems. *Biomed. Opt. Express* 12 (3), 1543–1558. doi:10.1364/boe.417345

Na, S., Russin, J. J., Lin, L., Yuan, X., Hu, P., Jann, K. B., et al. (2022a). Massively parallel functional photoacoustic computed tomography of the human brain. *Nat. Biomed. Eng.* 6 (5), 584–592. doi:10.1038/s41551-021-00735-8

Na, S., Russin, J. J., Lin, L., Yuan, X., Hu, P., Jann, K. B., et al. (2022b). Massively parallel functional photoacoustic computed tomography of the human brain. *Nat. Biomed. Eng.* 6 (5), 584–592. doi:10.1038/s41551-021-00735-8

Na, S., and Wang, L. V. (2021). Photoacoustic computed tomography for functional human brain imaging [Invited]. *Biomed. Opt. Express* 12 (7), 4056–4083. doi:10.1364/boe.423707

Nagao, R. J., Ouyang, Y., Keller, R., Nam, S. Y., Malik, G. R., Emelianov, S. Y., et al. (2016). Ultrasound-guided photoacoustic imaging-directed re-endothelialization of acellular vasculature leads to improved vascular performance. *Acta Biomater.* 32, 35–45. doi:10.1016/j.actbio.2015.12.029

Nam, S. Y., Chung, E., Suggs, L. J., and Emelianov, S. Y. (2015). Combined ultrasound and photoacoustic imaging to noninvasively assess burn injury and selectively monitor a regenerative tissue-engineered construct. *Tissue Eng. Part C-Methods* 21 (6), 557–566. doi:10.1089/ten.tec.2014.0306

Nam, S. Y., Ricles, L. M., Suggs, L. J., and Emelianov, S. Y. (2012). *In vivo* ultrasound and photoacoustic monitoring of mesenchymal stem cells labeled with gold nanotracers. *Plos One* 7 (5), e37267. doi:10.1371/journal.pone.0037267

Nelson, K. M., Reiber, G., Kohler, T., and Boyko, E. J. (2007). Peripheral arterial disease in a multiethnic national sample: the role of conventional risk factors and allostatic load. *Ethn. Dis.* 17 (4), 669–675.

Nenadic, I. Z., et al. (2019). *Ultrasound elastography for biomedical applications and medicine*. Hoboken: John Wiley and Sons.

Neuschler, E. I., Butler, R., Young, C. A., Barke, L. D., Bertrand, M. L., Böhm-Vélez, M., et al. (2018). A pivotal study of optoacoustic imaging to diagnose benign and malignant breast masses: a new evaluation tool for radiologists. *Radiology* 287 (2), 398–412. doi:10.1148/radiol.2017172228

Nie, L. M., Cai, X., Maslov, K., Garcia-Uribe, A., Anastasio, M. A., and Wang, L. V. (2012). Photoacoustic tomography through a whole adult human skull with a photon recycler. *J. Biomed. Opt.* 17 (11), 110506. doi:10.1117/1.jbo.17.11.110506

Niedre, M., and Ntziachristos, V. (2008). Elucidating structure and function *in vivo* with hybrid fluorescence and magnetic resonance imaging. *Proc. Ieee* 96 (3), 382–396. doi:10.1109/jproc.2007.913498

Ning, B., Sun, N., Cao, R., Chen, R., Kirk Shung, K., Hossack, J. A., et al. (2015a). Ultrasound-aided multi-parametric photoacoustic microscopy of the mouse brain. *Sci. Rep.* 5 (1), 18775. doi:10.1038/srep18775

Ning, B., Sun, N., Cao, R., Chen, R., Kirk Shung, K., Hossack, J. A., et al. (2015b). Ultrasound-aided multi-parametric photoacoustic microscopy of the mouse brain. *Sci. Rep.* 5, 18775. doi:10.1038/srep18775

Nyayapathi, N., Lim, R., Zhang, H., Zheng, W., Wang, Y., Tiao, M., et al. (2019). Dual scan mammoscope (DSM)—a new portable photoacoustic breast imaging system with scanning in craniocaudal plane. *IEEE Trans. Biomed. Eng.* 67 (5), 1321–1327. doi:10.1109/tbme.2019.2936088

Nyayapathi, N., and Xia, J. (2019). Photoacoustic imaging of breast cancer: a mini review of system design and image features. *J. Biomed. Opt.* 24 (12), 121911. doi:10.1117/1.jbo.24.12.121911

Nyayapathi, N., Zhang, H., Zheng, E., Nagarajan, S., Bonaccio, E., Takabe, K., et al. (2021). Photoacoustic dual-scan mammoscope: results from 38 patients. *Biomed. Opt. Express* 12 (4), 2054–2063. doi:10.1364/boe.420679

O Connor, J. P. B., Rose, C. J., Waterton, J. C., Carano, R. A., Parker, G. J., and Jackson, A. (2015). Imaging intratumor heterogeneity: role in therapy response, resistance, and clinical outcome. *Clin. Cancer Res.* 21 (2), 249–257. doi:10.1158/1078-0432.ccr-14-0990

Oeri, M., Bost, W., Sénégond, N., Tretbar, S., and Fournelle, M. (2017). Hybrid photoacoustic/ultrasound tomograph for real-time finger imaging. *Ultrasound Med. Biol.* 43 (10), 2200–2212. doi:10.1016/j.ultrasmedbio.2017.05.015

Oh, J. T., Zhang, H. F., Maslov, K., Stoica, G., and Wang, L. V. (2006). Three-dimensional imaging of skin melanoma *in vivo* by dual-wavelength photoacoustic microscopy. *J. Biomed. Opt.* 11 (3), 034032. doi:10.1117/1.2210907

Oraevsky, A., Clingman, B., Zalev, J., Stavros, A., Yang, W., and Parikh, J. (2018a). Clinical optoacoustic imaging combined with ultrasound for coregistered functional and anatomical mapping of breast tumors. *Photoacoustics* 12, 30–45. doi:10.1016/j.pacs.2018.08.003

Oraevsky, A., et al. (2018b). "Full-view 3D imaging system for functional and anatomical screening of the breast," in *Photons plus ultrasound: imaging and sensing* (USA: SPIE), 2018.

Ormachea, J., and Parker, K. J. (2020). Elastography imaging: the 30 year perspective. *Phys. Med. Biol.* 65. doi:10.1088/1361-6560/abca00

Park, B., Bang, C., Lee, C., Han, J., Choi, W., Kim, J., et al. (2021a). 3D wide-field multispectral photoacoustic imaging of human melanomas *in vivo*: a pilot study. *J. Eur. Acad. Dermatol Venereol.* 35 (3), 669–676. doi:10.1111/jdv.16985

Park, J., et al. (2020a). Seamlessly integrated optical and acoustical imaging systems through transparent ultrasonic transducer. *Photons Plus Ultrasound Imaging Sens.* 2020, 11240. doi:10.1117/12.2544037

Park, J., Park, B., Kim, T. Y., Jung, S., Choi, W. J., Ahn, J., et al. (2021b). Quadruple ultrasound, photoacoustic, optical coherence, and fluorescence fusion imaging with a transparent ultrasound transducer. *Proc. Natl. Acad. Sci.* 118 (11), e1920879118. doi:10.1073/pnas.1920879118

Park, J., Park, B., Kim, T. Y., Jung, S., Choi, W. J., Ahn, J., et al. (2021c). Quadruple ultrasound, photoacoustic, optical coherence, and fluorescence fusion imaging with a transparent ultrasound transducer. *Proc. Natl. Acad. Sci. U. S. A.* 118 (11), e1920879118. doi:10.1073/pnas.1920879118

Park, J., Park, B., Yong, U., Ahn, J., Kim, J. Y., Kim, H. H., et al. (2022). Bi-modal near-infrared fluorescence and ultrasound imaging via a transparent ultrasound transducer for sentinel lymph node localization: publisher's note. *Opt. Lett.* 47 (5), 1258. doi:10.1364/ol.454477

Park, S., Jang, J., Kim, J., Kim, Y. S., and Kim, C. (2017). Real-time triple-modal photoacoustic, ultrasound, and magnetic resonance fusion imaging of humans. *IEEE Trans. Med. Imaging* 36 (9), 1912–1921. doi:10.1109/tmi.2017.2696038

Park, S., Kang, S., and Chang, J. H. (2020b). Optically transparent focused transducers for combined photoacoustic and ultrasound microscopy. *J. Med. Biol. Eng.* 40 (5), 707–718. doi:10.1007/s40846-020-00536-5

Partridge, S. C., Ziadloo, A., Murthy, R., White, S. W., Peacock, S., Eby, P. R., et al. (2010). Diffusion tensor MRI: preliminary anisotropy measures and mapping of breast tumors. *J. Magnetic Reson. Imaging Official J. Int. Soc. Magnetic Reson. Med.* 31 (2), 339–347. doi:10.1002/jmri.22045

Pellacani, G., Cesinaro, A. M., and Seidenari, S. (2005). Reflectance-mode confocal microscopy of pigmented skin lesions--improvement in melanoma diagnostic specificity. *J. Am. Acad. Dermatol* 53 (6), 979–985. doi:10.1016/j.jaad.2005.08.022

Pesce, K., Orruma, M. B., Hadad, C., Bermúdez Cano, Y., Secco, R., and Cernadas, A. (2019). BI-RADS terminology for mammography reports: what residents need to know. *RadioGraphics* 39 (2), 319–320. doi:10.1148/rg.2019180068

Pierce, M. C., Schwarz, R. A., Bhattar, V. S., Mondrik, S., Williams, M. D., Lee, J. J., et al. (2012). Accuracy of *in vivo* multimodal optical imaging for detection of oral neoplasia. *Cancer Prev. Res.* 5 (6), 801–809. doi:10.1158/1940-6207.capr-11-0555

Pinhas-Hamiel, O., and Zeitler, P. (2005). The global spread of type 2 diabetes mellitus in children and adolescents. *J. Pediatr.* 146 (5), 693–700. doi:10.1016/j.jpeds.2004.12.042

Poelma, C. (2017). Ultrasound imaging velocimetry: a review. *Exp. Fluids* 58, 3–28. doi:10.1007/s00348-016-2283-9

Qiu, Q., Huang, Y., Zhang, B., Huang, D., Chen, X., Fan, Z., et al. (2022). Noninvasive dual-modality photoacoustic-ultrasonic imaging to detect mammalian embryo abnormalities after prenatal exposure to methylmercury chloride (MMC): a mouse study. *Environ. health Perspect.* 130 (2), 027002. doi:10.1289/ehp8907

Razansky, D., Klohs, J., and Ni, R. (2021). Multi-scale optoacoustic molecular imaging of brain diseases. *Eur. J. Nucl. Med. Mol. imaging* 48, 4152–4170. doi:10.1007/s00259-021-05207-4

Rebling, J., Estrada, H., Gottschalk, S., Sela, G., Zwack, M., Wissmeyer, G., et al. (2018a). Dual-wavelength hybrid optoacoustic-ultrasound biomicroscopy for functional imaging of large-scale cerebral vascular networks. *J. Biophot.* 11 (9), e201800057. doi:10.1002/jbio.201800057

Rebling, J., Estrada, H., Gottschalk, S., Sela, G., Zwack, M., Wissmeyer, G., et al. (2018b). Dual-wavelength hybrid optoacoustic-ultrasound biomicroscopy for functional imaging of large-scale cerebral vascular networks. *J. Biophot.* 11 (9), e201800057. doi:10.1002/jbio.201800057

Ren, D. Y., Sun, Y., Shi, J., and Chen, R. (2021). A review of transparent sensors for photoacoustic imaging applications. *Photonics* 8 (8), 324. doi:10.3390/photonics8080324

Richardson, P. D., Davies, M., and Born, G. (1989). Influence of plaque configuration and stress distribution on fissuring of coronary atherosclerotic plaques. *Lancet* 334 (8669), 941–944. doi:10.1016/s0140-6736(89)90953-7

Ricles, L. M., Nam, H., Sokolov, K., Emelianov, S., and Suggs, L. (2011). Function of mesenchymal stem cells following loading of gold nanotracers. *Int. J. Nanomedicine* 6, 407–416. doi:10.2147/ijn.s16354

Rofstad, E. K., Galappathi, K., Mathiesen, B., and Ruud, E. B. M. (2007). Fluctuating and diffusion-limited hypoxia in hypoxia-induced metastasis. *Clin. cancer Res.* 13 (7), 1971–1978. doi:10.1158/1078-0432.ccr-06-1967

Ronneberger, O., Fischer, P., and Brox, T. (2015). "U-net: convolutional networks for biomedical image segmentation," in *International Conference on Medical image computing and computer-assisted intervention* (Germany: Springer).

Saijo, Y., et al. (2019). Visualization of skin morphology and microcirculation with high frequency ultrasound and dual-wavelength photoacoustic microscope. *Photons Plus Ultrasound Imaging Sens.* 2019, 10878. doi:10.1117/12.2508599

Sandström, A., Altman, M., Cnattingius, S., Johansson, S., Ahlberg, M., and Stephansson, O. (2017). Durations of second stage of labor and pushing, and adverse neonatal outcomes: a population-based cohort study. *J. Perinatology* 37 (3), 236–242. doi:10.1038/jp.2016.214

Sarrion Perez, M. G., Bagán, J. V., Jiménez, Y., Margaix, M., and Marzal, C. (2015). Utility of imaging techniques in the diagnosis of oral cancer. *J. Craniomaxillofac Surg.* 43 (9), 1880–1894. doi:10.1016/j.jcms.2015.07.037

Schaar, J. A., et al. (2004). Terminology for high-risk and vulnerable coronary artery plaques. *Eur. heart J.* 25 (12), 1077–1082. doi:10.1016/j.ehj.2004.01.002

Schmidt, W. A. (2007). Technology Insight: the role of color and power Doppler ultrasonography in rheumatology. *Nat. Clin. Pract. Rheumatol.* 3 (1), 35–42. doi:10.1038/ncprheum0377

Schröder, F. H., Hugosson, J., Roobol, M. J., Tammela, T. L., Ciatto, S., Nelen, V., et al. (2009). Screening and prostate-cancer mortality in a randomized European study. *N. Engl. J. Med.* 360 (13), 1320–1328. doi:10.1056/nejmoa0810084

Schuurman, A.-S., Vroegindewey, M., Kardys, I., Oemrawsingh, R. M., Cheng, J. M., de Boer, S., et al. (2018). Near-infrared spectroscopy-derived lipid core burden index predicts adverse cardiovascular outcome in patients with coronary artery disease during long-term follow-up. *Eur. heart J.* 39 (4), 295–302. doi:10.1093/eurheartj/ehx247

Schwab, J., et al. (2019). "Deep learning of truncated singular values for limited view photoacoustic tomography," in *Photons plus ultrasound: imaging and sensing* (USA: SPIE), 2019.

Scotto di Santolo, M., Sagnelli, M., Mancini, M., Scalvenzi, M., Delfino, M., Schonauer, F., et al. (2015). High-resolution color-Doppler ultrasound for the study of skin growths. *Arch. Dermatol Res.* 307 (7), 559–566. doi:10.1007/s00403-015-1538-2

Seewaldt, V. (2014). ECM stiffness paves the way for tumor cells. *Nat. Med.* 20 (4), 332–333. doi:10.1038/nm.3523

Sen, C. K., Gordillo, G. M., Roy, S., Kirsner, R., Lambert, L., Hunt, T. K., et al. (2009). Human skin wounds: a major and snowballing threat to public health and the economy. *Wound repair Regen.* 17 (6), 763–771. doi:10.1111/j.1524-475x.2009.00543.x

Seth, D., Cheldize, K., Brown, D., and Freeman, E. E. (2017). Global burden of skin disease: inequities and innovations. *Curr. Dermatol. Rep.* 6 (3), 204–210. doi:10.1007/s13671-017-0192-7

Sheiham, A. (2005). Oral health, general health and quality of life. *Bull. World Health Organ* 83 (9), 644. doi:10.1111/j.1754-4505.2008.00045.x

Shin, E.-S., Garcia-Garcia, H. M., Ligthart, J. M. R., Witberg, K., Schultz, C., van der Steen, A. F., et al. (2011). *In vivo* findings of tissue characteristics using iMap™ IVUS and Virtual Histology™ IVUS. *EuroIntervention* 6 (8), 1017–1019. doi:10.4244/eijv6i8a175

Shrikhande, G. V., and McKinsey, J. F. (2012). *Diabetes and peripheral vascular disease: diagnosis and management*. Germany: Springer Science and Business Media.

Siegel, R. L., Miller, K. D., Fedewa, S. A., Ahnen, D. J., Meester, R. G. S., Barzi, A., et al. (2017). Colorectal cancer statistics, 2017. *A Cancer J. Clin.* 67 (3), 177–193. doi:10.3322/caac.21395

Siegel, R. L., Miller, K. D., and Jemal, A. (2019). Cancer statistics. *CA a cancer J. Clin.* 69 (1), 7–34. doi:10.3322/caac.21551

Stephens, K. (2021). FDA approves Seno medical's breast cancer diagnostic technology. *AXIS Imaging News*.

Stoffels, I., Jansen, P., Petri, M., Goerdt, L., Brinker, T. J., Griewank, K. G., et al. (2019). Assessment of nonradioactive multispectral optoacoustic tomographic imaging with conventional lymphoscintigraphic imaging for sentinel lymph node biopsy in melanoma. *JAMA Netw. Open* 2 (8), e199020. doi:10.1001/jamanetworkopen.2019.9020

Stoffels, I., Morscher, S., Helfrich, I., Hillen, U., Leyh, J., Burton, N. C., et al. (2015). Metastatic status of sentinel lymph nodes in melanoma determined noninvasively with multispectral optoacoustic imaging. *Sci. Transl. Med.* 7 (317), 317ra199. doi:10.1126/scitranslmed.aad1278

Su, J. L., Bouchard, R. R., Karpiouk, A. B., Hazle, J. D., and Emelianov, S. Y. (2011). Photoacoustic imaging of prostate brachytherapy seeds. *Biomed. Opt. express* 2 (8), 2243–2254. doi:10.1364/boe.2.002243

Subochev, P., Orlova, A., Shirmanova, M., Postnikova, A., and Turchin, I. (2015). Simultaneous photoacoustic and optically mediated ultrasound microscopy: an *in vivo* study. *Biomed. Opt. Express* 6 (2), 631–638. doi:10.1364/boe.6.000631

Sun, Y., Xie, H., Liu, J., Lam, M., Chaudhari, A. J., Zhou, F., et al. (2012). *In vivo* validation of a bimodal technique combining time-resolved fluorescence spectroscopy and ultrasonic backscatter microscopy for diagnosis of oral carcinoma. *J. Biomed. Opt.* 17 (11), 116003. doi:10.1117/1.jbo.17.11.116003

Swetter, S. M. (2003). Dermatological perspectives of malignant melanoma. *Surg. Clin. North Am.* 83 (1), 77–95. doi:10.1016/s0039-6109(02)00091-9

Szabo, T. L. (2004). *Diagnostic ultrasound imaging: inside out*. Massachusetts: Academic Press.

Tai, H., Khairalseed, M., and Hoyt, K. (2020). Adaptive attenuation correction during H-scan ultrasound imaging using K-means clustering. *Ultrasonics* 102, 105987. doi:10.1016/j.ultras.2019.105987

Tanaka, K., and Sata, M. (2018). Roles of perivascular adipose tissue in the pathogenesis of atherosclerosis. *Front. physiology* 9, 3. doi:10.3389/fphys.2018.00003

Tang, Y., Dong, Z., Wang, N., Del Aguila, A., Johnston, N., Vu, T., et al. (2023). Non-invasive deep-brain imaging with 3D integrated photoacoustic tomography and ultrasound localization microscopy (3D-PAULM). *ArXiv*, arXiv:2307.14572v1. doi:10.48550/arXiv.2307.14572

Tanter, M., and Fink, M. (2014). Ultrafast imaging in biomedical ultrasound. *IEEE Trans. ultrasonics, Ferroelectr. Freq. control* 61 (1), 102–119. doi:10.1109/tuffc.2014.6689779

Tegnander, E., and Eik-Nes, S. H. (2006). The examiner's ultrasound experience has a significant impact on the detection rate of congenital heart defects at the second-trimester fetal examination. *Ultrasound Obstet. Gynecol.* 28 (1), 8–14. doi:10.1002/uog.2804

Torre, L. A., Trabert, B., DeSantis, C. E., Miller, K. D., Samimi, G., Runowicz, C. D., et al. (2018). Ovarian cancer statistics. *CA a cancer J. Clin.* 68 (4), 284–296. doi:10.3322/caac.21456

Uppot, R. N. (2018). Technical challenges of imaging and image-guided interventions in obese patients. *Br. J. Radiology* 91 (1089), 20170931. doi:10.1259/bjr.20170931

van den Berg, P. J., Daoudi, K., Bernelot Moens, H. J., and Steenbergen, W. (2017). Feasibility of photoacoustic/ultrasound imaging of synovitis in finger joints using a point-of-care system. *Photoacoustics* 8, 8–14. doi:10.1016/j.pacs.2017.08.002

VanderLaan, D., Karpiouk, A. B., Yeager, D., and Emelianov, S. (2017). Real-time intravascular ultrasound and photoacoustic imaging. *IEEE Trans. Ultrasonics, Ferroelectr. Freq. Control* 64 (1), 141–149. doi:10.1109/tuffc.2016.2640952

van Es, P., Vlieg, R. C., Hondebrink, E., van Hespen, J. C. G., Bernelot Moens, H. J., Steenbergen, W., et al. (2015). Coregistered Photoacoustic and ultrasound tomography of healthy and inflamed human interphalangeal joints. *Opto-Acoustic Methods Appl. Biophot. Ii*, 9539. doi:10.1364/ecbo.2015.95390c

Vannucci, R. C. (2000). Hypoxic-ischemic encephalopathy. *Am. J. perinatology* 17 (03), 113–120. doi:10.1055/s-2000-9293

van Soest, G., Marcu, L., Bouma, B. E., and Regar, E. (2017). Intravascular imaging for characterization of coronary atherosclerosis. *Curr. Opin. Biomed. Eng.* 3, 1–12. doi:10.1016/j.cobme.2017.07.001

Verhagen, S. N., and Visseren, F. L. (2011). Perivascular adipose tissue as a cause of atherosclerosis. *Atherosclerosis* 214 (1), 3–10. doi:10.1016/j.atherosclerosis.2010.05.034

Virmani, R., Kolodgie, F. D., Burke, A. P., Finn, A. V., Gold, H. K., Tulenko, T. N., et al. (2005). Atherosclerotic plaque progression and vulnerability to rupture: angiogenesis as a source of intraplaque hemorrhage. *Arterioscler Thromb Vasc Biol.* 25 (10), 2054–2061. doi:10.1161/01.atv.0000178991.71605.18

Wang, B., Su, J. L., Amirian, J., Litovsky, S. H., Smalling, R., and Emelianov, S. (2010a). Detection of lipid in atherosclerotic vessels using ultrasound-guided spectroscopic intravascular photoacoustic imaging. *Opt. express* 18 (5), 4889–4897. doi:10.1364/oe.18.004889

Wang, B., Su, J. L., Karpiouk, A. B., Sokolov, K. V., Smalling, R. W., and Emelianov, S. Y. (2010b). Intravascular photoacoustic imaging. *IEEE J. Sel. Top. Quantum Electron.* 16 (3), 588–599. doi:10.1109/jstqe.2009.2037023

Wang, C., Chen, X., Wang, L., Makihata, M., Liu, H. C., Zhou, T., et al. (2022). Bioadhesive ultrasound for long-term continuous imaging of diverse organs. *Science* 377 (6605), 517–523. doi:10.1126/science.abo2542

Wang, C. C., Guo, L., Wang, G., Ye, T., Wang, B., Xiao, J., et al. (2021). *In-vivo* imaging of melanoma with simultaneous dual-wavelength acoustic-resolution-based photoacoustic/ultrasound microscopy. *Appl. Opt.* 60 (13), 3772–3778. doi:10.1364/ao.412609

Wang, L., Xia, J., Yao, J., and Maslov, K. I. (2013). Ultrasonically encoded photoacoustic flowgraphy in biological tissue. *Phys. Rev. Lett.* 111 (20), 204301. doi:10.1103/physrevlett.111.204301

Wang, L. V. (2008a). Prospects of photoacoustic tomography. *Med. Phys.* 35 (12), 5758–5767. doi:10.1118/1.3013698

Wang, L. V. (2008b). Tutorial on photoacoustic microscopy and computed tomography. *IEEE J. Sel. Top. Quantum Electron.* 14 (1), 171–179. doi:10.1109/jstqe.2007.913398

Wang, L. V. (2009). Multiscale photoacoustic microscopy and computed tomography. *Nat. photonics* 3 (9), 503–509. doi:10.1038/nphoton.2009.157

Wang, L. V. (2017). *Photoacoustic imaging and spectroscopy*. Florida: CRC Press.

Wang, L. V., and Hu, S. (2012). Photoacoustic tomography: *in vivo* imaging from organelles to organs. *Science* 335 (6075), 1458–1462. doi:10.1126/science.1216210

Wang, P., Wang, H. W., and Cheng, J. X. (2012). Mapping lipid and collagen by multispectral photoacoustic imaging of chemical bond vibration. *J. Biomed. Opt.* 17 (9), 0960101. doi:10.1117/1.jbo.17.9.096010

Wang, S., Zhao, Y., and Xu, Y. (2020). Recent advances in applications of multimodal ultrasound-guided photoacoustic imaging technology. *Vis. Comput. Ind. Biomed. Art.* 3 (1), 24. doi:10.1186/s42492-020-00061-x

Wang, Y. T., Xu, D., Yang, S., and Xing, D. (2016). Toward *in vivo* biopsy of melanoma based on photoacoustic and ultrasound dual imaging with an integrated detector. *Biomed. Opt. Express* 7 (2), 279–286. doi:10.1364/boe.7.000279

Wang, Z., Tao, W., and Zhao, H. (2023b). The optical inverse problem in quantitative photoacoustic tomography: a review. *Photonics* 10, 487. doi:10.3390/photonics10050487

Wang, Z., Tong, Z., Chen, H., Nie, G., Hu, J., Liu, W., et al. (2023a). Photoacoustic/ultrasonic dual-mode imaging for monitoring angiogenesis and synovial erosion in rheumatoid arthritis. *Photoacoustics* 29, 100458. doi:10.1016/j.pacs.2023.100458

Watson, N. J. (2022). "Ultrasound tomography," in *Industrial tomography* (Germany: Elsevier), 245–273.

Wen, Y., Guo, D., Zhang, J., Liu, X., Liu, T., et al. (2022). Clinical photoacoustic/ultrasound dual-modal imaging: current status and future trends. *Front. Physiol.* 13, 1036621. doi:10.3389/fphys.2022.1036621

Wu, C., and Bayer, C. L. (2018). Imaging placental function: current technology, clinical needs, and emerging modalities. *Phys. Med. Biol.* 63 (14), 14TR01. doi:10.1088/1361-6560/aaccd9

Wu, D., Huang, L., Jiang, M., and Jiang, H. (2014). Contrast agents for photoacoustic and thermoacoustic imaging: a review. *Int. J. Mol. Sci.* 15 (12), 23616–23639. doi:10.3390/ijms151223616

Wu, M., Springeling, G., Lovrak, M., Mastik, F., Iskander-Rizk, S., Wang, T., et al. (2017). Real-time volumetric lipid imaging *in vivo* by intravascular photoacoustics at 20 frames per second. *Biomed. Opt. Express* 8 (2), 943–953. doi:10.1364/boe.8.000943

Wu, X., Sanders, J. L., Zhang, X., Yamaner, F. Y., and Oralkan, O. (2019). An FPGA-based backend system for intravascular photoacoustic and ultrasound imaging. *IEEE Trans. Ultrasonics, Ferroelectr. Freq. Control* 66 (1), 45–56. doi:10.1109/tuffc.2018.2881409

Xia, J., Danielli, A., Liu, Y., Wang, L., Maslov, K., and Wang, L. V. (2013a). Calibration-free quantification of absolute oxygen saturation based on the dynamics of photoacoustic signals. *Opt. Lett.* 38 (15), 2800–2803. doi:10.1364/ol.38.002800

Xia, J., Huang, C., Maslov, K., Anastasio, M. A., and Wang, L. V. (2013b). Enhancement of photoacoustic tomography by ultrasonic computed tomography based on optical excitation of elements of a full-ring transducer array. *Opt. Lett.* 38 (16), 3140–3143. doi:10.1364/ol.38.003140

Xia, J., Yao, J., and Wang, L. V. (2014). PHOTOACOUSTIC tomography: PRINCIPLES and advances (invited review). *Prog. Electromagn. Res.* 147, 1–22. doi:10.2528/pier14032303

Xia, W., et al. (2016). "Interventional multispectral photoacoustic imaging with a clinical linear array ultrasound probe for guiding nerve blocks," in *Photons plus ultrasound: imaging and sensing* (USA: SPIE), 2016.

Xu, G., Rajian, J. R., Girish, G., Kaplan, M. J., Fowlkes, J. B., Carson, P. L., et al. (2013). Photoacoustic and ultrasound dual-modality imaging of human peripheral joints. *J. Biomed. Opt.* 18 (1), 010502. doi:10.1117/1.jbo.18.1.010502

Xu, J., Cheng, X., Chen, F., Li, W., Xiao, X., Lai, P., et al. (2021). Fabrication of multifunctional polydopamine-coated gold nanobones for PA/CT imaging and enhanced synergistic chemo-photothermal therapy. *J. Mater. Sci. Technol.* 63, 97–105. doi:10.1016/j.jmst.2020.04.060

Yamaleyeva, L. M., Brosnihan, K. B., Smith, L. M., and Sun, Y. (2018). Preclinical ultrasound-guided photoacoustic imaging of the placenta in normal and pathologic pregnancy. *Mol. Imaging* 17, 153601211880272. doi:10.1177/1536012118802721

Yamaleyeva, L. M., Sun, Y., Bledsoe, T., Hoke, A., Gurley, S. B., and Brosnihan, K. B. (2017). Photoacoustic imaging for *in vivo* quantification of placental oxygenation in mice. *FASEB J.* 31 (12), 5520–5529. doi:10.1096/fj.201700047rr

Yan, Y., Hernandez-Andrade, E., Basij, M., Alshahrani, S. S., Kondle, S., Brown, B. O., et al. (2021). *Endocavity ultrasound and photoacoustic system for fetal and maternal imaging: design, implementation, and ex-vivo validation*. *J. Med. Imaging* 8 (6), 066001. doi:10.1117/1.jmi.8.6.066001

Yang, C., Lan, H., Gao, F., and Gao, F. (2021). Review of deep learning for photoacoustic imaging. *Photoacoustics* 21, 100215. doi:10.1016/j.pacs.2020.100215

Yang, J., Zhang, G., Shang, Q., Wu, M., Huang, L., and Jiang, H. (2020). Detecting hemodynamic changes in the foot vessels of diabetic patients by photoacoustic tomography. *J. Biophot.* 13 (8), e202000011. doi:10.1002/jbio.202000011

Yang, M., Zhao, L., He, X., Su, N., Zhao, C., Tang, H., et al. (2017). Photoacoustic/ultrasound dual imaging of human thyroid cancers: an initial clinical study. *Biomed. Opt. express* 8 (7), 3449–3457. doi:10.1364/boe.8.003449

Yao, J., and Wang, L. V. (2013). Photoacoustic microscopy. *Laser and Photonics Rev.* 7 (5), 758–778. doi:10.1002/lpor.201200060

Ye, J., Fu, Q., Liu, L., Chen, L., Zhang, X., Li, Q., et al. (2021). Ultrasound-propelled Janus Au NR-mSiO2 nanomotor for NIR-II photoacoustic imaging guided sonodynamic-gas therapy of large tumors. *Sci. China Chem.* 64 (12), 2218–2229. doi:10.1007/s11426-021-1070-6

Yelin, E., Weinstein, S., and King, T. (2016). The burden of musculoskeletal diseases in the United States. *Seminars Arthritis Rheumatism* 46 (3), 259–260. doi:10.1016/j.semarthrit.2016.07.013

Yildiz, F., Matsunaga, T., and Haga, Y. (2018). Fabrication and packaging of CMUT using low temperature Co-fired ceramic. *Micromachines* 9 (11), 553. doi:10.3390/mi9110553

Yin, J., Tao, C., Cai, P., and Liu, X. (2015). Photoacoustic tomography based on the Green's function retrieval with ultrasound interferometry for sample partially behind an acoustically scattering layer. *Appl. Phys. Lett.* 106 (23), 234101. doi:10.1063/1.4922386

Yuan, J., Xu, G., Yu, Y., Zhou, Y., Carson, P. L., Wang, X., et al. (2013). Real-time photoacoustic and ultrasound dual-modality imaging system facilitated with graphics processing unit and code parallel optimization. *J. Biomed. Opt.* 18 (8), 086001–086001. doi:10.1117/1.JBO.18.8.086001

Zhang, E. Z., Povazay, B., Laufer, J., Alex, A., Hofer, B., Pedley, B., et al. (2011). Multimodal photoacoustic and optical coherence tomography scanner using an all optical detection scheme for 3D morphological skin imaging. *Biomed. Opt. express* 2 (8), 2202–2215. doi:10.1364/boe.2.002202

Zhang, H., Bo, W., Wang, D., DiSpirito, A., Huang, C., Nyayapathi, N., et al. (2021). Deep-E: a fully-dense neural network for improving the elevation resolution in linear-array-based photoacoustic tomography. *IEEE Trans. Med. Imaging* 41 (5), 1279–1288. doi:10.1109/tmi.2021.3137060

Zhang, H., Li, H., Nyayapathi, N., Wang, D., Ying, L., et al. (2020). A new deep learning network for mitigating limited-view and under-sampling artifacts in ring-shaped photoacoustic tomography. *Comput. Med. Imaging Graph.* 84, 101720. doi:10.1016/j.compmedimag.2020.101720

Zhang, J., Yang, S., Ji, X., Zhou, Q., and Xing, D. (2014). Characterization of lipid-rich aortic plaques by intravascular photoacoustic tomography: *ex vivo* and *in vivo* validation in a rabbit atherosclerosis model with histologic correlation. *J. Am. Coll. Cardiol.* 64 (4), 385–390. doi:10.1016/j.jacc.2014.04.053

Zhang, L., and Wang, X. (2022). Optical resolution photoacoustic microscopy imaging in the detection of early oral cancer under image reconstruction algorithm. *Comput. Math. Methods Med.* 2022, 1–11. doi:10.1155/2022/6077748

Zhao, C., Zhang, R., Zhu, Q., Wang, M., Yang, M., and Jiang, Y. (2021b). The potential of photoacoustic techniques in inflammatory arthritis: what can it do to assist conventional imaging methods? *Chin. J. Acad. Radiology* 4 (2), 79–87. doi:10.1007/s42058-021-00066-2

Zhao, C. Y., Wang, Q., Tao, X., Wang, M., Yu, C., Liu, S., et al. (2021a). Multimodal photoacoustic/ultrasonic imaging system: a promising imaging method for the evaluation of disease activity in rheumatoid arthritis. *Eur. Radiol.* 31 (5), 3542–3552. doi:10.1007/s00330-020-07353-z

Zheng, E., Zhang, H., Goswami, S., Kabir, I. E., Doyley, M. M., and Xia, J. (2021). Second-generation dual scan mammoscope with photoacoustic, ultrasound, and elastographic imaging capabilities. *Front. Oncol.* 11, 11. doi:10.3389/fonc.2021.779071

Zhong, H., Duan, T., Lan, H., Zhou, M., and Gao, F. (2018). Review of low-cost photoacoustic sensing and imaging based on laser diode and light-emitting diode. *Sensors* 18 (7), 2264. doi:10.3390/s18072264

Zhou, Y., Yao, J., and Wang, L. (2016). Tutorial on photoacoustic tomography. *J. Biomed. Opt.* 21 (6), 061007. doi:10.1117/1.jbo.21.6.061007

Zhu, Q. (2022). A review of co-registered transvaginal photoacoustic and ultrasound imaging for ovarian cancer diagnosis. *Curr. Opin. Biomed. Eng.* 22, 100381. doi:10.1016/j.cobme.2022.100381

Zhu, Y., Feng, T., Cheng, Q., Wang, X., Du, S., Sato, N., et al. (2020). Towards clinical translation of LED-based photoacoustic imaging: a review. *Sensors* 20 (9), 2484. doi:10.3390/s20092484

Zloković, B. V., Segal, M. B., Begley, D. J., Davson, H., and Rakić, L. (1985). Permeability of the blood-cerebrospinal fluid and blood-brain barriers to thyrotropin-releasing hormone. *Brain Res.* 358 (1-2), 191–199. doi:10.1016/0006-8993(85)90963-1